

Characterization of Markarian 421 during its most violent year: Multiwavelength variability and correlations

K. Abe¹, S. Abe², J. Abhir³, A. Abhishek⁴, V. A. Acciari⁵, A. Aguasca-Cabot⁶, I. Agudo⁷, T. Aniello⁸, S. Ansoldi^{9,42}, L. A. Antonelli⁸, A. Arbet Engels^{10*}, C. Arcaro¹¹, K. Asano², D. Baack¹², A. Babić¹³, U. Barres de Almeida¹⁴, J. A. Barrio¹⁵, I. Batković¹¹, A. Bautista¹⁰, J. Baxter², J. Becerra González¹⁶, W. Bednarek¹⁷, E. Bernardini¹¹, J. Bernete¹⁸, A. Berti¹⁰, J. Besenrieder¹⁰, C. Bigongiari⁸, A. Biland³, O. Blanch⁵, G. Bonnoli⁸, Ž. Bošnjak¹³, E. Bronzini⁸, I. Burelli⁹, A. Campoy-Ordaz¹⁹, R. Carosi²⁰, M. Carretero-Castrillo⁶, A. J. Castro-Tirado⁷, D. Cerasole²¹, G. Ceribella¹⁰, Y. Chai², A. Cifuentes¹⁸, E. Colombo⁵, J. L. Contreras¹⁵, J. Cortina¹⁸, S. Covino⁸, G. D'Amico²², F. D'Ammando⁴⁸, V. D'Elia⁸, P. Da Vela⁸, F. Dazzi⁸, A. De Angelis¹¹, B. De Lotto⁹, R. de Menezes²³, M. Delfino^{5,43}, J. Delgado^{5,43}, C. Delgado Mendez¹⁸, F. Di Piero²³, R. Di Tria²¹, L. Di Venere²¹, D. Dominis Prester²⁴, A. Donini⁸, D. Dorner²⁵, M. Doro¹¹, L. Eisenberger²⁵, D. Elsaesser¹², J. Escudero⁷, L. Fariña⁵, A. Fattorini¹², L. Foffano⁸, L. Font¹⁹, S. Fröse¹², S. Fukami³, Y. Fukazawa²⁶, R. J. García López¹⁶, M. Garczarczyk²⁷, S. Gasparyan²⁸, M. Gaug¹⁹, J. G. Giesbrecht Paiva¹⁴, N. Giglietto²¹, F. Giordano²¹, P. Gliwny¹⁷, N. Godinović²⁹, T. Gradetzke¹², R. Grau⁵, D. Green¹⁰, J. G. Green¹⁰, P. Günther²⁵, D. Hadasch², A. Hahn¹⁰, T. Hassan¹⁸, L. Heckmann¹⁰, J. Herrera Llorente¹⁶, D. Hrupec³⁰, R. Imazawa²⁶, K. Ishio¹⁷, I. Jiménez Martínez¹⁰, J. Jormanainen³¹, S. Kankkunen³¹, T. Kayanoki²⁶, D. Kerszberg⁵, G. W. Kluge^{22,44}, P. M. Kouch³¹, H. Kubo², J. Kushida¹, M. Láinez¹⁵, A. Lamastra⁸, F. Leone⁸, E. Lindfors³¹, S. Lombardi⁸, F. Longo^{9,45}, R. López-Coto⁷, M. López-Moya¹⁵, A. López-Oramas¹⁶, S. Loporchio²¹, A. Lorini⁴, P. Majumdar³², M. Makariev³³, G. Maneva³³, M. Manganaro²⁴, S. Mangano¹⁸, K. Mannheim²⁵, M. Mariotti¹¹, M. Martínez⁵, M. Martínez-Chicharro¹⁸, A. Mas-Aguilar¹⁵, D. Mazin^{2,10}, S. Menchiari⁷, S. Mender¹², D. Miceli¹¹, T. Miener¹⁵, J. M. Miranda⁴, R. Mirzoyan¹⁰, M. Molero González¹⁶, E. Molina¹⁶, H. A. Mondal³², A. Moralejo⁵, D. Morcuende⁷, T. Nakamori³⁴, C. Nanci⁸, V. Neustroev³⁵, L. Nickel¹², C. Nigro⁵, L. Nikolić⁴, K. Nilsson³¹, K. Nishijima¹, T. Njoh Ekoume⁵, K. Noda³⁶, S. Nozaki¹⁰, A. Okumura³⁷, J. Otero-Santos⁷, S. Paiano⁸, D. Paneque^{10*}, R. Paoletti⁴, J. M. Paredes⁵, M. Peresano¹⁰, M. Persic^{9,46}, M. Pihet¹¹, G. Pirola¹⁰, F. Podobnik⁴, P. G. Prada Moroni²⁰, E. Prandini¹¹, G. Principe⁹, W. Rhode¹², M. Ribó⁶, J. Rico⁵, C. Righi⁸, N. Sahakyan²⁸, T. Saito², F. G. Saturni⁸, K. Schmidt¹², F. Schmuckermaier^{10*}, J. L. Schubert¹², T. Schweizer¹⁰, A. Sciacaluga⁸, G. Silvestri¹¹, J. Sitarek¹⁷, D. Sobczynska¹⁷, A. Stamerra⁸, J. Striško³⁰, D. Strom¹⁰, Y. Suda²⁶, H. Tajima³⁷, M. Takahashi³⁷, R. Takeishi², F. Tavecchio⁸, P. Temnikov³³, K. Terauchi³⁸, T. Terzić²⁴, M. Teshima^{10,47}, S. Truzzi⁴, A. Tutone⁸, S. Ubach¹⁹, J. van Scherpenberg¹⁰, S. Ventura⁴, G. Verna⁴, I. Viale¹¹, C. F. Vigorito²³, V. Vitale³⁹, I. Vovk², R. Walter⁴⁰, F. Wersig¹², M. Will¹⁰, T. Yamamoto⁴¹, S. G. Jorstad⁴⁹, A. P. Marscher⁴⁹, M. Perri^{50,51}, C. Leto⁵², F. Verrecchia^{50,51}, M. Aller⁵³, W. Max-Moerbeck⁵⁴, A. C. S. Readhead^{55,56}, A. Lähteenmäki^{57,58}, M. Tornikoski⁵⁷, and M. A. Gurwell⁵⁹ A. E. Wehrle⁶⁰

(Affiliations can be found after the references)

Received XX XX, 2023; accepted XX XX, 2023

ABSTRACT

Aims. Mrk 421 was in its most active state around early 2010, which led to the highest TeV gamma-ray flux ever recorded from any active galactic nuclei (AGN). We aim to characterize the multiwavelength behavior during this exceptional year for Mrk 421, and evaluate whether it is consistent with the picture derived with data from other less exceptional years.

Methods. We investigated the period from November 5, 2009, (MJD 55140) until July 3, 2010, (MJD 55380) with extensive coverage from very-high-energy (VHE; $E > 100$ GeV) gamma rays to radio with MAGIC, VERITAS, *Fermi*-LAT, *RXTE*, *Swift*, GASP-WEBT, VLBA, and a variety of additional optical and radio telescopes. We characterized the variability by deriving fractional variabilities as well as power spectral densities (PSDs). In addition, we investigated images of the jet taken with VLBA and the correlation behavior among different energy bands.

Results. Mrk 421 was in widely different states of activity throughout the campaign, ranging from a low-emission state to its highest VHE flux ever recorded. We find the strongest variability in X-rays and VHE gamma rays, and PSDs compatible with power-law functions with indices around 1.5. We observe strong correlations between X-rays and VHE gamma rays at zero time lag with varying characteristics depending on the exact energy band. We also report a marginally significant ($\sim 3\sigma$) positive correlation between high-energy (HE; $E > 100$ MeV) gamma rays and the ultraviolet band. We detected marginally significant ($\sim 3\sigma$) correlations between the HE and VHE gamma rays, and between HE gamma rays and the X-ray, that disappear when the large flare in February 2010 is excluded from the correlation study, hence indicating the exceptionality of this flaring event in comparison with the rest of the campaign. The 2010 violent activity of Mrk421 also yielded the first ejection of features in the VLBA images of the jet of Mrk 421. Yet the large uncertainties in the ejection times of these unprecedented radio features prevent us from firmly associating them to the specific flares recorded during the 2010 campaign. We also show that the collected multi-instrument data are consistent with a scenario where the emission is dominated by two regions, a compact and extended zone, which could be considered as a simplified implementation of an energy-stratified jet as suggested by recent *IXPE* observations.

Key words. BL Lacertae objects: individual: Mrk 421 galaxies: active gamma rays: general radiation mechanisms: nonthermal

1. Introduction

Blazars are a class of jetted active galactic nuclei (AGN). The relativistic plasma jet is oriented with a small angle with respect to the line of sight. Blazars emit across the full electromagnetic spectrum, ranging from radio to high-energy (HE; $E > 100$ MeV) and very-high-energy (VHE; $E > 100$ GeV) gamma rays. Blazars that show no or very faint emission lines in their optical emission are referred to as BL Lac-type objects (Urry & Padovani 1995).

The broadband emission of BL Lac-type objects is dominated by non-thermal radiation from the jet. The spectral energy distribution (SED) exhibits two large features in the form of two large bumps (see e.g. Abdo et al. 2011). Measurements of spectral and polarization characteristics strongly indicate that the first bump originates from synchrotron radiation produced by relativistic electrons and positrons moving in the magnetic field within the jet. The origin of the second bump is still under debate and is more difficult to determine. Possible leptonic scenarios include electron inverse Compton (IC) scattering on synchrotron photons originating from the first bump, so called synchrotron self-Compton (SSC) (Maraschi et al. 1992; Ghisellini et al. 1998; Madejski et al. 1999), or in certain cases additionally on external target photons (Dermer et al. 1992; Sikora et al. 1994). Hadronic scenarios can also provide explanations for the gamma-ray emission (Mannheim 1993; Mücke & Protheroe 2001; Cerruti et al. 2015). BL Lac-type objects can be classified by their peak frequency of the synchrotron bump (Urry & Padovani 1995; Padovani et al. 2017; Abdo et al. 2010a). Blazars with a peak frequency of $\nu_s < 10^{14}$ Hz are referred to as low synchrotron peaked blazars (LSPs), with a peak frequency 10^{14} Hz $< \nu_s < 10^{15}$ Hz as intermediate synchrotron peaked blazars (ISPs) and with $\nu_s > 10^{15}$ Hz as high synchrotron peaked blazars (HSPs).

Markarian 421 (Mrk 421; RA=11^h4'27.31'', Dec=38°12'31.8'', J2000, $z=0.031$) is an archetypal and very close HSP. It is among the most studied sources in the VHE sky. Mrk 421 was found in states of extreme activity in the X-ray and VHE gamma-ray bands during previous campaigns (e.g. Gaidos et al. 1996; Fossati et al. 2008; Aleksić et al. 2015c; Acciari et al. 2020; Abeysekara et al. 2020). Among all campaigns, 2010 stands out as the most active and violent year seen in the VHE emission from Mrk 421. In February 2010, the Very Energetic Radiation Imaging Telescope Array System (VERITAS) detected the highest VHE flux recorded to date from Mrk 421 (Abeysekara et al. 2020). The highest flux measurement reached a level of ~ 27 Crab Units (C.U.) above 1 TeV, making it the brightest VHE gamma-ray flux ever recorded for an AGN. The high photon statistic during such flaring activity allowed for a binning of the flux in 2-minute intervals. A cross-correlation study with the optical band revealed a significant positive correlation with a time lag of ~ 25 -55 minutes. Additional correlation studies between the VHE and X-ray bands showed a complex and fast-varying correlation from linear to quadratic behavior down to no correlation at times. Shortly after, in March 2010, a decaying flare was detected by the Florian Goebel Major Atmospheric Gamma Imaging Cherenkov (MAGIC) and VERITAS telescopes (Aleksić et al. 2015c). The detailed and broad multiwavelength (MWL) coverage enabled the construction of 13 consecutive daily SEDs. The emission could be successfully modeled by a single-SSC zone. However, as described in Aleksić et al. (2015c), a better model-data agreement and a more natural explanation of the SED evolution

could be achieved with a two-zone scenario. The variation of only a few model parameters could successfully describe the SED variation and made the underlying particle population a very plausible cause of the variable emission.

For the first time, this work exploits the full campaign covering a time period spanning from November 2009 until June 2010 with a broad MWL coverage. High-resolution radio data taken with the Very Long Baseline Interferometry (VLBI) technique add observations of the jet structure to the campaign from mid January 2010 to early July 2012. This wealth of data allows for a detailed study of the variability and correlation behavior of Mrk 421 during its most violent recorded year.

2. Multiwavelength light curves

The study involves data from several instruments covering the emission from radio frequencies to VHE in the time period from November 5, 2009, (MJD 55140) until July 3, 2010, (MJD 55380). The key instruments used are MAGIC, VERITAS, the Large Area Telescope (LAT) on board the *Fermi Gamma-ray Space Telescope* (*Fermi*-LAT), the X-Ray telescope (XRT) and the Ultra-violet Optical Telescope (UVOT) on board the *Neil Gehrels Swift Observatory* (*Swift*) and the GLAST-AGILE Support Program - Whole Earth Blazar Telescope (GASP-WEBT) network of optical telescopes. Additional telescopes in the X-ray, optical and radio support these. The details of the data analysis of the individual instruments are given in the Appendix in Sec. A.

The top row of Fig. 1 shows the light curves provided by the MAGIC telescopes in the 0.2-1 TeV and >1 TeV band. For comparison, multiples of the flux of the Crab Nebula¹ are given with dashed-dotted lines. At the beginning of the campaign in November 2009, Mrk 421 was already in an elevated state of activity with an emission of around 1 C.U. in both bands. The average emission state of the source estimated by Whipple over a time span of 14 years is around 0.45 C.U. (Acciari et al. 2014). After a small gap of observations, Mrk 421 showed a strong flaring activity reaching over 3 C.U. above 1 TeV in January 2010. The emission showed strong variability by up to a factor of almost three on a daily timescale. We found significant intranight variability on January 15 (see Appendix C). After a short phase at around 1 C.U., another observational gap due to adverse weather conditions is present in the MAGIC telescope data. Following the gap, a decaying flare starting at around 2 C.U. could be observed, which is discussed in great detail in Aleksić et al. (2015c). Mrk 421 showed average emission for the following two months until it entered an especially low emission state around June, going below 0.25 C.U..

The second row shows the combined VHE light curve provided by MAGIC and VERITAS on a logarithmic scale. Due to the additional VERITAS data, the gap in February 2010 is covered. These observations yielded the largest VHE flux observed to date in an AGN, reaching almost 10 C.U. for the daily average. Using a shorter binning, the peak flux values reached ~ 15 C.U. above 200 GeV (Abeysekara et al. 2020).

The third row displays the emission in high-energy gamma rays (HE; $E > 100$ MeV) measured by *Fermi*-LAT in a three-day binning in the 0.3 GeV to 3 GeV and 3 GeV to 300 GeV band. During the large VHE flare in February, both bands show increased emission and reached their highest flux coincident with the highest VHE flux point. The other two VHE flares during

* Corresponding authors: F. Schmuckermaier, D. Paneque, A. Arbet-Engels, e-mail: contact.magic@mpp.mpg.de

¹ The flux of the Crab Nebula used in this work is taken from Aleksić et al. (2016)

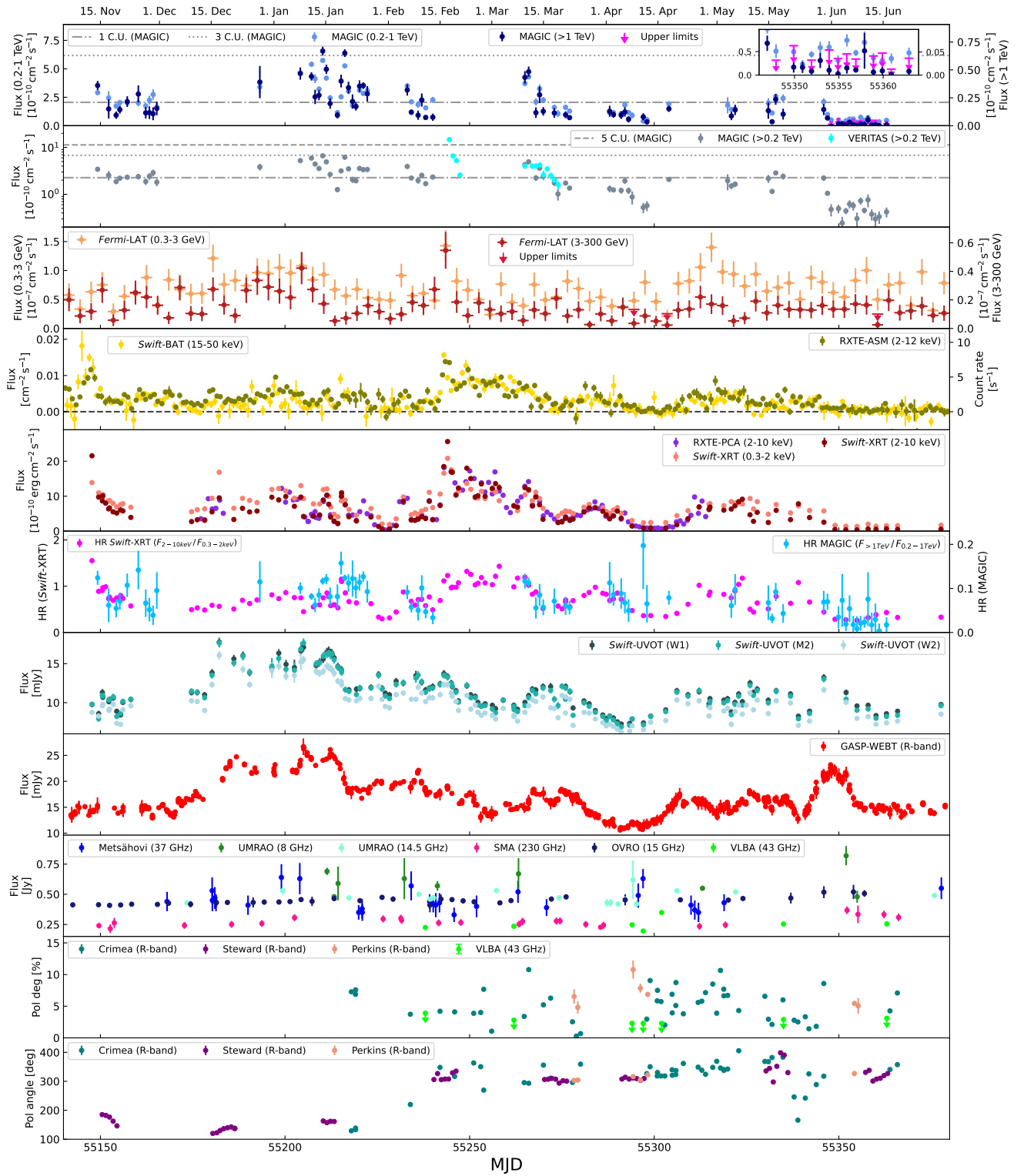


Fig. 1: MWL light curves covering the time period from November 5, 2009, (MJD 55140) to July 3, 2010, (MJD 55380). Top to bottom: MAGIC fluxes in daily bins for two energy bands (note the two different y-axes); VHE fluxes obtained from MAGIC and VERITAS above 0.2 TeV (in log scale); *Fermi*-LAT fluxes in 3-day bins in two energy bands; X-ray fluxes in 1-day bins from the all-sky monitors *Swift*-BAT and *RXTE*-ASM; X-ray fluxes from the pointing instruments *Swift*-XRT and *RXTE*-PCA; hardness ratio between the high and low-energy fluxes of *Swift*-XRT and between the two VHE bands of MAGIC (note the two different y-axes); optical R-band data from GASP-WEBT; radio data from Metsähovi, UMR AO, SMA, OVRO and VLBA; polarization degree and polarization angle observations in the optical from the Steward and Perkins observatories and in radio from VLBA.

121 January and March do not show increased activity in HE gamma
122 rays. We additionally checked if daily binning reveals any activ-

ity on a shorter scale during these two flares that might be hidden
with a 3-day binning but did not find significant variability.

123
124

In the fourth and fifth rows, the results of the X-ray are shown. A short outburst is detected in November 2009, around MJD 55145. The flare fades over a few days, and the source remains at a comparably lower activity level without any noticeable outbursts. Coinciding with the VHE flare in February, all wavebands show a sharp increase in flux, which slowly decreases in the following month. At the end of the campaign, the X-ray emission also entered a remarkably low state.

Using the two separate VHE and X-ray light curves, hardness ratios (i.e. the ratio of the flux in the higher-energy band to the flux in the lower-energy band) can be obtained and are shown in row six. Overall, the source showed a harder-when-brighter trend in VHE and X-ray, which has been observed frequently in the past (e.g. Acciari et al. 2021; MAGIC Collaboration et al. 2021). This behavior is investigated in more detail in Appendix D.

Row seven and eight contain the UV and optical fluxes, respectively. Due to the closeness in frequency, the trends are quite similar. Both light curves reach their highest emission coincident to the January VHE flare. When the subsequent February flare starts, there is no clear visible flare in the UV or optical.

The ninth row shows the fluxes obtained from radio observations. The instruments cover a variety of frequencies, which makes flux comparisons challenging. Overall, the source showed a low activity and a low variability in all radio bands.

The second to last row reports the polarization degree, which shows some strong fluctuations throughout the campaign, going from values as low as 0.3% up to $\sim 11\%$ around a mean of $\sim 5\%$. The corresponding electric vector polarization angles (EVPA) in the optical are shown in the last row. The data were adjusted for the intrinsic 180° ambiguity as reported in Carnerero et al. (2017). The EVPA shows a constant behavior at the beginning at around $\sim 150^\circ$ followed by a wide rotation happening around MJD 55230 (early February). For the remaining campaign, it fluctuates around $\sim 350^\circ$. Since the EVPA rotates by around 200° during a time interval with very limited coverage (only one measurement), one cannot completely exclude that this rotation arises from an improper correction of the 180° ambiguity. If the rotation is real, there might be a possible connection with the large flare in February at higher energies.

3. VLBA observations of the jet evolution

Fig. 2 shows the total intensity VLBA images of Mrk 421 from May 2010 to August 2011. The images are shown from May onwards when the ejection of the first feature is observed. The source structure was modeled using a number of emission components (knots) with circular Gaussian brightness distributions. Based on their parameters, we identify knots across the epochs. The brightest knot located at the southern end of the jet is the VLBI core at 43 GHz, which we place at zero distance in Fig. 2. The core, designated as A0, is assumed to be a stationary physical structure of the jet. Another (quasi-)stationary feature is located at 0.38 ± 0.06 mas from the core, labeled A1. At the distance of Mrk 421, one can use the conversion scale $0.638 \text{ pc mas}^{-12}$ to convert the angular distance of 0.38 mas into a physical distance of 0.24 pc. During the observations, two new components emerged from the core, K1 and K2. The components were already reported in Jorstad et al. (2017) (K1 and K2

² from the NASA/IPAC Extragalactic Database, <https://ned.ipac.caltech.edu/>

are referred to as B1 and B2, respectively). As reported there, the existence of B1 (K1 in this manuscript) as a real knot is not absolutely certain. All average parameters of the components (i.e. names of the knot, number of epochs at which the knot is detected, flux density, distance from the core, position angle with respect to the core, and the size of the knot) are listed in Tab. 1. The corresponding kinematic properties of K1 and K2 are listed in Tab. 2 (Phi refers to the speed direction). The newly emerging component K1 moves at a speed of 0.78 mas/yr, which corresponds to an apparent speed of $1.56 \pm 0.45 c$, making it just about a superluminal knot (note the large uncertainty). K2 moves much slower with a speed of 0.16 mas/yr corresponding to $0.32 \pm 0.07 c$.

Fig. 3 shows the angular distance from the core of the components A1, K1, and K2, as a function of time. Since A1 is identified as a stationary feature, the distance versus time of A1 with respect to A0 is fit with a horizontal line, while separations of two new components from the core are approximated by linear fits with the best χ^2 value. This allows us to determine times of ejection (passage through the center of the core) of K1 and K2 by extrapolation of the motion of knots back to the core position (see Tab. 2).

K1 is ejected at $\text{MJD } 55112 \pm 88$ and K2 at $\text{MJD } 55400 \pm 157$. Both ejection times fall well within the main period of this work, shown in light gray, from MJD 55140 to 55380 within their one-sigma band. Because of the large uncertainties, however, it is impossible to establish a connection with a particular event, such as one of the three VHE flares, marked with solid gray lines.

Nevertheless, it is remarkable that in the period Mrk 421 exhibited the most violent behavior with three large VHE flares, including the brightest flare ever, the ejection of two new components was seen right after. Despite VLBA components having been identified for a few TeV-emitting blazars (mostly FSRQs), a potential association of gamma-ray flares with the ejection and propagation of knots is rarely observed in HSPs (Weaver et al. 2022). To our knowledge, this is the only time the ejection of new components in the jet of Mrk 421 was observed. Previous works only found stationary or already present subluminal knots (e.g. Piner & Edwards 2005; Lico et al. 2012; Richards et al. 2013; Blasi et al. 2013).

4. Variability

4.1. Fractional variability

In order to estimate the degree of variability in each energy band, we use the fractional variability F_{var} as it is described in Vaughan et al. (2003). The estimation of the uncertainties follows the description in Aleksić et al. (2015a), which uses the approach from Poutanen et al. (2008). Fig. 4 shows the resulting fractional variability using the full light curves in open markers. The full markers show the results for quasi-simultaneous data. We define quasi-simultaneity as the temporal agreement with VHE data within 6 h for X-ray and UV data. The choice of 6 h is a compromise between having sufficient data and not too much loss of temporal coincidence. We use a window of 1 day for optical data and 3 days for radio and Fermi-LAT data.

In both cases, a pronounced two-peak structure is visible, indicating the highest variability in the X-ray and VHE. Similar behavior has been observed multiple times for Mrk 421 (e.g. Aleksić et al. 2015b; Baloković et al. 2016; MAGIC Collaboration et al. 2021). As mentioned in Sec. 1, the typical SED from a blazar such as Mrk 421 shows a double bump structure (Abdo et al. 2011), where the first bump is electron synchrotron emis-

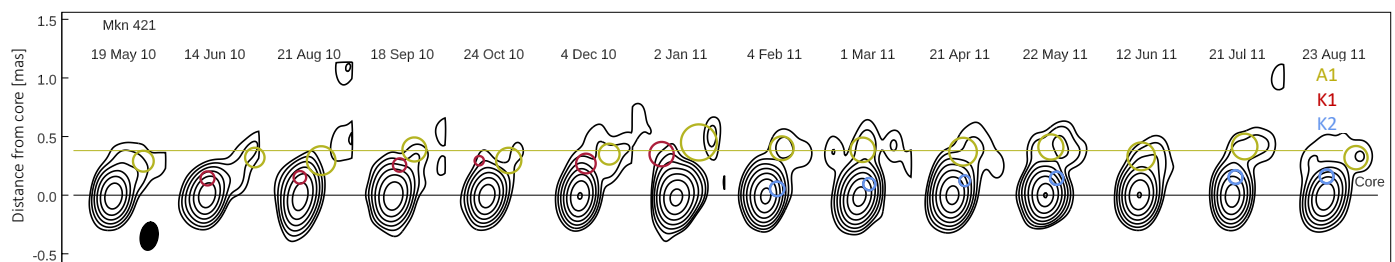


Fig. 2: Total intensity VLBA images from May 2010 to August 2011. The black and yellow lines show the average positions of the stationary features A0 and A1. The yellow, red and blue circles show the fitted positions of A1, K1, and K2, respectively.

Table 1: Average parameters of the features shown in Fig. 2

Component	Number of epochs	Flux (Jy)	Distance (mas)	Theta (deg)	Size (FWHM,mas)
A0	31	0.210 ± 0.048	0.0	...	0.072 ± 0.030
A1	24	0.025 ± 0.012	0.378 ± 0.062	-28.9 ± 14.3	0.267 ± 0.117
K1	5	0.011 ± 0.008	0.29 ± 0.18	-34.2 ± 27.2	0.146 ± 0.131
K2	8	0.060 ± 0.005	0.20 ± 0.12	-37.3 ± 7.6	0.145 ± 0.036

Table 2: Kinematic properties of the knots K1 and K2.

Knot	Proper motion (mas/yr)	Phi (deg)	Apparent speed (c)	Ejection time (yr)	Ejection time (MJD)
K1	0.775 ± 0.225	49.5 ± 15.2	1.56 ± 0.45	2009.77 ± 0.24	55112 ± 88
K2	0.157 ± 0.033	-21.8 ± 20	0.32 ± 0.07	2010.56 ± 0.43	55400 ± 157

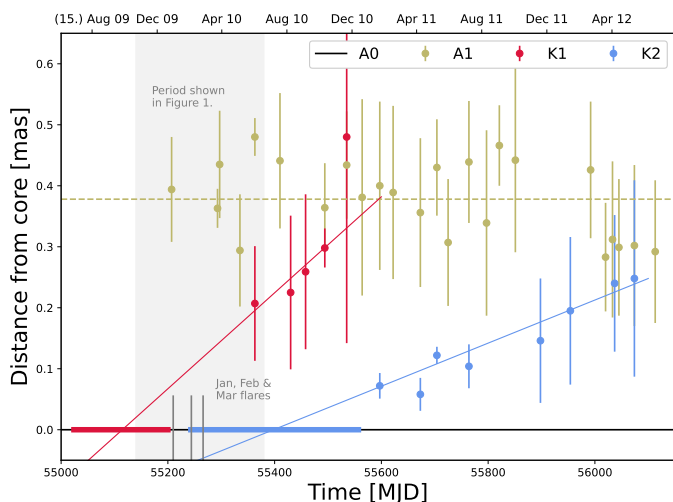


Fig. 3: Angular distance of A1 (yellow), K1 (red), and K2 (blue) from the jet core (black). At the location of Mrk 421, the angular distance of one mas is equivalent to a physical distance of 0.638 pc. The dotted yellow line indicates a constant fit of the quasi-stationary component. The red and blue lines show linear fits to determine the time of ejection of the components. The uncertainties on the ejection times are given by the red and blue bands. The campaign of this work is given by the light gray band with the three flares marked with gray lines.

In the context of a SSC model, the same electrons produce the second bump of the SED in the gamma rays via inverse Compton emission. A similar variability pattern is therefore also expected in the variability of the gamma-ray peak. Fig. 4 shows the same degree of variability at TeV energies as in keV energies. This result already suggests the existence of a correlation between the two wavebands, which is investigated in more detail in Sec. 5.

4.2. Power spectral density

Additionally, we investigate the variability of Mrk 421 with the use of the power spectral density (PSD). The PSD quantifies the amplitude of the variability as a function of the timescale of the variations. It is based on the discrete Fourier transform of a light curve. The typical shape of the PSD for blazars follows a simple power law $P_\nu \propto \nu^{-a}$ with the spectral index a ranging between 1 and 2 (e.g. Uttley et al. 2002; Chatterjee et al. 2008; Abdo et al. 2010b). A falling power law indicates a large variability at long timescales (small frequencies), and the power of this variability decreases as one considers shorter and shorter timescales (high frequencies).

Our method of estimating the PSD indices is described in Appendix B, and the results obtained are reported in Table 3. We find values for the PSD indices that are well compatible within their uncertainties with the ones derived in Aleksić et al. (2015b). Due to the larger uncertainties of the light curve, the PSD indices for the *Fermi*-LAT bands are not well constrained and show noticeably smaller values. We did not find evidence of a spectral break of the PSD index in any energy band. In addition, we used the Lomb-Scargle method (Lomb 1976; Scargle 1982) to search for signs of periodicity but found no evidence in our data set.

244 sion. The falling edge of that bump, covered by the X-rays, is
245 emitted by the most freshly accelerated and energetic electrons,
246 which also have the shortest cooling times, meaning high vari-
247 ability. At energies below the X-rays, the electrons responsi-
248 ble for the synchrotron emission have lower energies and hence
249 longer cooling times, resulting in a strong decrease in variability.

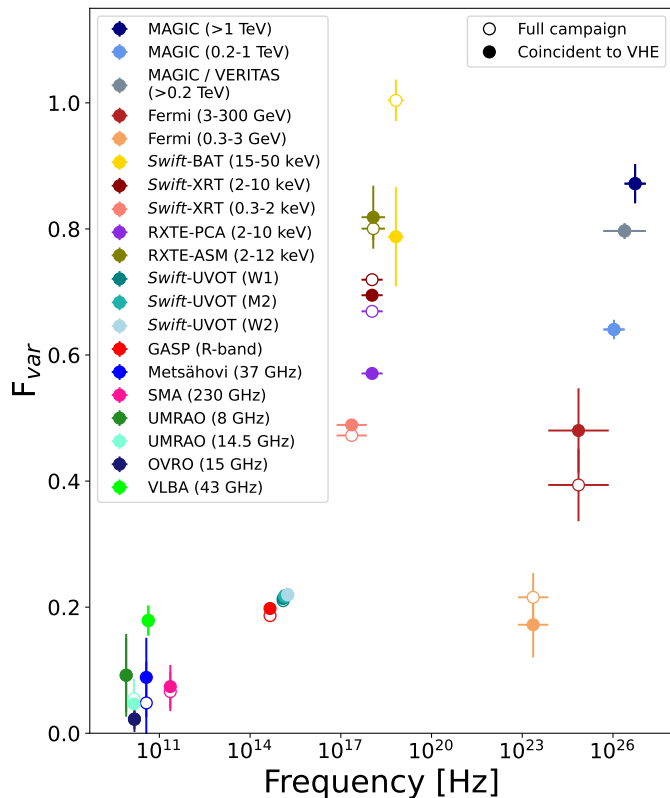


Fig. 4: Fractional variability F_{var} as a function of the frequency for the light curves shown in Fig. 1. Open markers show the results using the whole campaign for each light curve. Full markers only include quasi-simultaneous data to the VHE data (quasi-simultaneity is defined as temporal agreement with VHE data within 6 h for X-ray and UV data, within 1 day for optical data, and within 3 days for radio and *Fermi-LAT* data.)

Table 3: PSD index best fit a for each energy band.

Energy band (instrument)	Best fit a
> 1 TeV (MAGIC)	$1.4^{+0.4}_{-0.3}$
0.2-1 TeV (MAGIC)	$1.5^{+0.5}_{-0.3}$
> 0.2 TeV (MAGIC/VERITAS)	$1.5^{+0.5}_{-0.2}$
3-300 GeV (<i>Fermi-LAT</i>)	$0.8^{+1.0}_{-0.6}$
0.3-3 GeV (<i>Fermi-LAT</i>)	$0.4^{+0.8}_{-0.3}$
15-50 keV (<i>Swift-BAT</i>)	$1.3^{+0.2}_{-0.2}$
2-10 keV (<i>Swift-XRT</i>)	$1.4^{+0.2}_{-0.2}$
0.3-2 keV (<i>Swift-XRT</i>)	$1.4^{+0.2}_{-0.2}$
W1 (<i>Swift-UVOT</i>)	$1.6^{+0.3}_{-0.3}$
R-band (GASP-WEBT)	$1.9^{+0.3}_{-0.2}$

5. Correlation studies

5.1. VHE gamma rays versus X-rays

The VHE gamma rays and the X-rays are the two energy bands where Mrk 421 shows the highest flux variations (as displayed in Fig. 4), which can occur on timescales as short as hours (see

Appendix C). Because of that, the observing campaign was organized with a special focus on maximizing the simultaneity between the VHE gamma rays and X-ray measurements. Hence, the collected dataset allows us to investigate the correlations with a large number of VHE gamma rays and X-ray measurements taken within a time window of only a few hours. Previous works investigated the source behavior either during a low state of activity (Baloković et al. 2016), a typical state of activity (MAGIC Collaboration et al. 2021) or during a flaring activity (Acciari et al. 2020). The large variability shown by Mrk 421 during the MWL campaign in 2010 allows us to probe the correlation behavior across all states of emission within a single campaign lasting about half a year. Since we did not find a time delay between the two bands, we evaluate the data at zero time lag and with a flux-flux plot within a time window of only 6 hours. Fig. 5 shows the the fluxes (in decimal logarithmic scale) of all three VHE bands versus the fluxes of the two *Swift-XRT* bands and the one provided by *Swift-BAT*.

In order to evaluate the degree of correlation, we use the Pearson coefficient using the pairs of flux data shown in Fig. 5, but without applying the decimal logarithm. We quantify the significance of the correlation using dedicated Monte-Carlo simulations. The methods are described in Appendix E. We find strong correlations between all VHE and *Swift-XRT* energy bands. In all six panels, we find Pearson coefficients equal or above 0.75 with significances ranging from slightly above 3 up to 4 σ . The correlation between the VHE and the *Swift-BAT* band is much weaker, reaching coefficients around 0.4-0.5 and significances around 2 σ . The significance of the correlation may be reduced by the large flux uncertainties of the BAT measurements (in comparison to the small uncertainties in the flux measurements from XRT).

We investigate the correlation slopes by fitting lines to the decimal logarithm of the data shown in the scatter plots. Since we did not find a significant change in the correlation slope over time by fitting individual ~ 1 month periods, we show a single line fit for the whole campaign. It is noteworthy that in the subplots between the >0.2 TeV flux with both X-ray bands, the observations of the highest and lowest X-ray flux lie well on the linear fit. This indicates a linear trend reaching over a full order of magnitude of emission and on the timescale of multiple months. The steepest slope (1.5 ± 0.2) is obtained for the highest VHE gamma-ray band versus the lowest X-ray band, while the flattest slope (0.3 ± 0.1) is obtained for the lowest VHE gamma-ray band versus highest X-ray band. Overall, the slope is increasing with rising VHE energy, showing a greater scaling of the >1 TeV flux with rising X-ray fluxes. Additionally, the slope decreases with rising X-ray energy. The same trends have been found in MAGIC Collaboration et al. (2021) as well, but the absolute slope values were found to be greater, reaching a cubic relation in some cases.

5.2. VHE gamma rays versus UV

The *Swift-UVOT* instrument has the same data coverage in the UV as *Swift-XRT* in X-rays. This allows us to follow the same approach as in the previous section to investigate a possible correlation between the VHE and UV band pairs. Fig. 6 shows the decimal logarithm of the fluxes of all three VHE bands versus the flux of the W1 filter (all three UV filters provide almost identical results, and we have selected W1 as a representative for all correlations). The values for the Pearson coefficient range from around 0.45 to 0.65 for all three panels, indicating a much weaker correlation. However, the corresponding significances of these correlations are all around 2 σ , and hence, this result

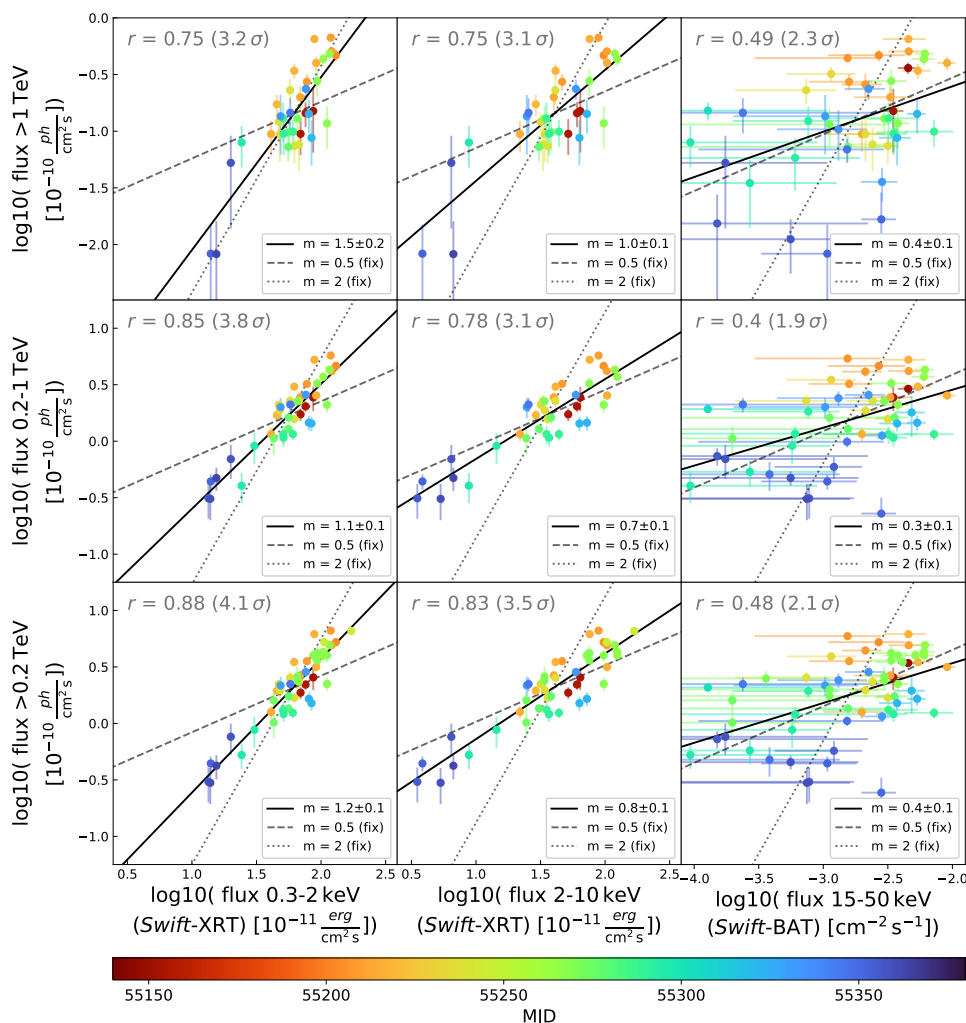


Fig. 5: VHE flux versus X-ray flux obtained by MAGIC/VERITAS and *Swift*-XRT/BAT. Only pairs of observations within 6 hours are considered. If more than one *Swift* observation falls within that window, the weighted mean is computed. VHE fluxes are in the >1 TeV band (top panels), in the 0.2-1 TeV band (middle panels), and in the >0.2 TeV band (bottom panels). *Swift*-XRT fluxes are computed in the 0.3-2 keV (left panels) and 2-10 keV bands (middle panels). *Swift*-BAT provides the flux in the 15-50 keV band (right panels). The top left corner of each panel shows the Pearson coefficient of the flux pairs, with the significance of the correlations given in parentheses. The gray dashed and dotted lines depict a fit with slope fixed to 0.5 and 2, respectively, and the black line is the best-fit line to the data, with the slope quoted in the legend at the bottom right of each panel.

347 should be considered as a hint of correlation. If the correlation
348 were real, this would be the first time, to our knowledge, that a
349 positive correlation between VHE gamma rays and the UV band
350 is found.

351 For the linear fits, we obtain compatible values of around
352 $m=2$ for all three panels. Due to the higher dispersion of the
353 data, the uncertainties of the fit are rather large. The higher slope
354 indicates a steeper correlation of the VHE with UV compared
355 to X-rays. Since the degree of variability is much higher in the
356 VHE than the UV (see Fig. 4), the flux varies substantially more,
357 and a steeper slope is expected in the case of a correlation.

358 5.3. VHE versus HE gamma rays

359 Next, we investigate the correlation between the two energy
360 bands in gamma rays using the combined light curve above
361 0.2 TeV from MAGIC and VERITAS. We correlate the bands using
362 the DCF without rebinning the LCs. We use a 3-day binned
363 time lag in the range of -40 to +40 days. The significance of

the resulting DCF is estimated with simulations similar to the
364 approach in MAGIC Collaboration et al. (2021): We first simu-
365 late a set of 10000 uncorrelated light curves for a pair of energy
366 bands as before. We then compute the DCF of the 10000 simu-
367 lated light curve pairs. The 1σ , 2σ and 3σ confidence bands
368 are derived from the distribution of the simulated DCF values in
369 each time lag bin.
370

The result for the DCFs between the >0.2 TeV band with
371 the 3-300 GeV band is shown in Fig. F.1a. The figure shows the
372 DCF obtained from the data in dark blue. The DCF peaks at a
373 time lag of 2 ± 2 days, where it crosses the 3σ line. To estimate
374 the uncertainty of the time lag, we follow the method outlined
375 in Peterson et al. (1998).
376

We note that the marginally significant (a little over 3σ) peak
377 at zero time lag is primarily driven by the big flare in February
378 2010 because the highest flux points in the VHE and HE light
379 curves occur during this flare. If the highest flux in the HE light
380 curve (that relates to a 3-day time interval from MJD 55242.0
381 to MJD 55245.0 or 2010-02-15 00:00 to 2010-02-18 00:00), to-
382

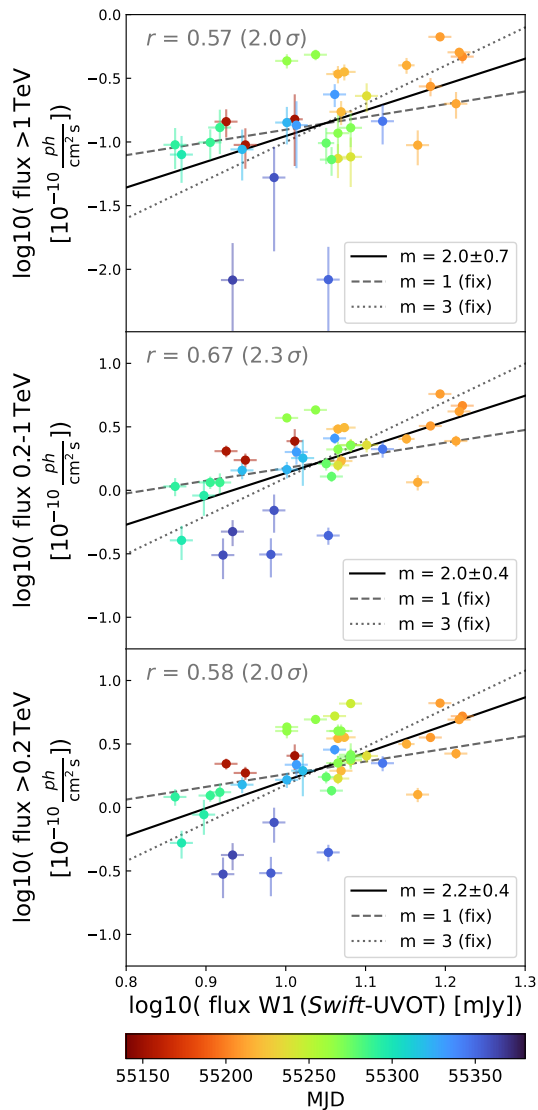


Fig. 6: VHE flux versus UV flux obtained by MAGIC/VERITAS and *Swift*-UVOT. Only pairs of observations within 6 hours are considered. If more than one *Swift* observation falls within that window, the weighted mean is computed. VHE fluxes are in the >1 TeV band (top panels), in the 0.2-1 TeV band (middle panels) and in the >0.2 TeV band (bottom panels). The *Swift*-UVOT fluxes are taken with the W1 filter. The top left corner of each panel shows the Pearson coefficient of the flux pairs, with the significance of the correlations given in parentheses. The gray dashed and dotted lines depict a fit with slope fixed to 0.5 and 2, respectively, and the black line is the best-fit line to the data, with the slope quoted in the legend at the bottom right of each panel.

383 together with the corresponding VHE fluxes in this 3-day time in-
 384 terval, are removed from the DCF study, the correlation at zero
 385 time lag vanishes, as shown in Fig. F.1b. A similar behavior is
 386 seen in the correlation between the >0.2 TeV band and the 0.3-
 387 3 GeV band, as it is also shown in Figs. F.1c and F.1d. But this
 388 time, the significance of the peak at zero time lag is just over the
 389 2σ line, even including the 2010 February flare.

5.4. HE gamma rays versus X-rays

390

For the correlation between HE gamma rays from *Fermi*-LAT 391
 and X-rays from *Swift*-XRT, we again use the DCF. We correlate 392
 each of the two HE gamma-ray bands with each of the X-ray 393
 bands from *Swift*-XRT. Here, we only display the strongest cor- 394
 relation as an example, which is found between the 3-300 GeV 395
 and the 0.3-2 keV band, shown in Fig. F.2a. A correlation peak 396
 lying above 3σ is found at a time lag of -1 ± 2 days. Similar 397
 to the VHE versus HE gamma-ray case, the sharp peak at zero 398
 time lag is likely dominated by the outstanding flaring activity on 399
 February 17. Fig. F.2b shows the same correlation but with the 400
 flare removed from both the light curves taken by *Fermi*-LAT, as 401
 well as the simultaneous flux in the X-ray light curve. The high 402
 peak at exactly zero time lag vanishes, but a broad peak remains. 403

The other three combinations of energy bands (0.3-3 GeV 404
 versus 0.2-3 keV, 3-300 GeV versus 2-10 keV, 0.3-3 GeV versus 405
 2-10 keV) are also shown in Fig. F.2. In all combinations, one 406
 can see a marginally significant peak at a time lag of about zero 407
 that disappears when removing the 3-day LAT flux bin (and cor- 408
 responding X-ray fluxes) from the outstanding flaring activity 409
 around 2010 February 17. The period in early 2010, including 410
 the flare, marks the first time such a correlation was observed, as 411
 previously reported in Abeysekara et al. (2020). 412

5.5. HE gamma rays versus UV

413

Fig. F.3a shows the DCF between the 3-300 GeV and the UV 414
 bands. It exhibits a broad peak crossing the 3σ line, and it 415
 reaches its highest value at a time lag of -7 ± 6 days. Between 416
 the 0.3-3 GeV band and the UV in Fig. F.3c, the highest value 417
 at -1 ± 6 days also reaches a significance level above 3σ . The 418
 positive correlation between both HE gamma-ray regions and 419
 the UV band is a novel behavior for Mrk 421 with no previous 420
 reports to our knowledge. Acciari et al. (2021) found a positive 421
 correlation compatible with a time lag of zero between the 0.3- 422
 300 GeV band, and the R-band, which frequency is close to the 423
 UV. The correlation was found by investigating the time period 424
 2007-2016 with a 15-day binning resulting in a lower temporal 425
 resolution than the one used here. 426

Contrary to the previous cases, the correlation between HE 427
 gamma-rays and the UV increases if the flare in February is ex- 428
 cluded. Figs. F.3b and F.3d show the results of correlating the 429
 HE gamma-ray light curves with the UV light curve without the 430
 flare. In the case of 3-300 GeV, the peak is clearly enlarged, go- 431
 ing well above 3σ , indicating a stronger correlation than before. 432
 For 0.3-3 GeV, the improvement is only marginal. The peaks re- 433
 main at the same time lag as before. 434

5.6. HE gamma rays versus R-band

435

We additionally test whether the correlation between the HE 436
 gamma rays and the optical as previously reported in Acciari 437
 et al. (2021) is also present in our data set. Fig. F.4 shows the 438
 DCF for the R-band and the two HE bands, which does not lead 439
 to any significantly correlated behavior, apart from a marginally 440
 significant ($\sim 3\sigma$) feature at about -35 days. 441

Removing the 3-day interval that contains the large VHE 442
 and X-ray flare in February 2010 does not change substantially 443
 the shape and the significance of the DCF results for these two 444
 bands. Only a marginal increase to 2.5σ is seen for the 3- 445
 300 GeV versus optical (see Fig. F.4b). 446

447 5.7. Other energy bands

448 We also investigated the correlation behavior between all other
449 wavebands not mentioned in the previous sections. We found no
450 correlation (positive or negative) between any bands in the X-ray
451 with the UV or the optical. Previous works have found anti-
452 correlated behavior at times (e.g. [MAGIC Collaboration et al.](#)
453 [2021](#); [Abe et al. 2023](#)), which was not present in our data set.
454 Naturally, there is a strong correlation between the UV and optical,
455 as the energy is close to each other. Since we established
456 a hint of a correlation between VHE and UV, we also checked
457 if a correlation is present between the VHE and the optical. Ap-
458 plying the same method, we find no correlations at all between
459 VHE and optical. We also found no correlation of any sort be-
460 tween radio and other energy bands. Due to the limited duration
461 of the campaign (about seven months), the overall number of ra-
462 dio observations is also relatively small, in comparison to studies
463 that used multi-year datasets (see e.g. [Camerero et al. 2017](#); [Ac-
464 ciari et al. 2021](#)). In addition, the synchrotron self-absorption of
465 radio radiation might reduce any detectable correlation.

466 6. Discussion

467 6.1. First detection of ejection of radio knots 468 contemporaneous to a flare of Mrk 421

469 VLBA observations reveal the ejection of two features in the jet
470 that are close in time to the observed VHE gamma-ray flares
471 (see Sect. 3). While the association of the ejection and propa-
472 gation of bright knots in the jet with gamma-ray flares has been
473 observed repeatedly in blazars, the vast majority of these detec-
474 tions were reported in FSRQs (like PKS 1510-089) or LSP and
475 ISP BL Lacertae (see [Jorstad et al. 2001](#); [Marscher et al. 2008](#);
476 [MAGIC Collaboration et al. 2018](#)). The association has rarely
477 been observed in HSPs, and this is the first time for Mrk 421 (see
478 e.g. the sample in [Weaver et al. 2022](#)), hence making the dataset
479 presented in this paper unique on its own. However, the large
480 uncertainties of the ejection time prevent us from significantly
481 correlating the appearance of the radio features with the spe-
482 cific VHE gamma-ray flares during this campaign. We also note
483 that previous works on Mrk 421 reported a possible connection
484 between GeV gamma-ray and radio flares detected with single-
485 dish telescopes ([Hovatta et al. 2015](#)). However, this large GeV
486 flaring activity, which was measured with *Fermi*-LAT in the year
487 2012, and the exceptionally large radio flare, which was (mostly)
488 measured with OVRO also in 2012, was not associated with the
489 ejection of features in the VLBA images ([Richards et al. 2013](#)).
490 Hence, they can have a different nature, and are not comparable
491 to the ejection of features in the VLBA images during the 2010
492 campaign that is reported in this manuscript.

493 Assuming the flare in February is indeed correlated with
494 the ejection of the radio features, the VHE intranight variabil-
495 ity implies a small, compact zone responsible for the emission
496 based on causality arguments. As discussed in [Abeysekara et al.](#)
497 [\(2020\)](#), following [Dondi & Ghisellini \(1995\)](#), the intranight vari-
498 ability down to 22 min at VHE in February 2010 allows us to
499 derive a lower limit on the Doppler factor of $\delta_{\min} \gtrsim 33$ based on
500 opacity arguments.

501 [Jorstad et al. \(2017\)](#) estimate the average Doppler factor de-
502 rived from VLBA observations to be around 24, hence below
503 the lower limit mentioned above using the VHE observations.
504 This regularly observed discrepancy between the observed jet
505 kinematics in the radio and the Doppler factors derived from the
506 fast variability at high energies is referred to as the *Doppler cri-*

507 *sis*. This could potentially be resolved by the presence of struc-
508 tured jets, in which different regions show different Lorentz fac-
509 tors, such as a fast spine responsible for the gamma-ray emis-
510 sion and a slower sheath layer responsible for the radio emis-
511 sion ([Ghisellini et al. 2005](#)). Recent works also proposed a sce-
512 nario in which the discrepancy is reconciled by assuming, on the
513 one hand, a large viewing angle relative to the jet explaining the
514 slow-moving knot in radio, while on the other hand, the gamma-
515 ray flare originates from a magnetic reconnection event within
516 a misaligned layer that effectively generates large Doppler fac-
517 tors ([Jormanainen et al. 2023](#)). Finally, jet deceleration occur-
518 ring between the time of the gamma-ray flare and the detection
519 of the radio feature may partly solve this crisis ([Georganopoulos
& Kazanas 2003](#)).

520 The FWHM of the radio knots reported in Sect. 3 is in the
521 order of 0.15 mas (both for K1 and K2). At the distance of
522 Mrk 421, this corresponds to a linear size of roughly $0.1 \text{ pc} \approx$
523 $3 \times 10^{17} \text{ cm}$ (0.638 pc/mas). Assuming a Doppler factor of 33
524 and a variability timescale of 22 minutes, the upper limit to the
525 size of the emitting region during the VHE flare is in the order
526 of 10^{15} cm ([Abeysekara et al. 2020](#)). If one again postulates that
527 the radio knot corresponds to the same region that produced the
528 VHE flare in February 2010, this implies an expansion veloc-
529 ity in the comoving frame of the emitting region in the order
530 of $\beta_{exp} = 10^{-2}c$ (using a time difference between the gamma-
531 ray flare and the radio detection of roughly 300 days, as one can
532 infer from Fig. 3). It is interesting to note that such expansion
533 velocity is well in line with the estimates of [Tramacere et al.](#)
534 [\(2022\)](#), which are obtained when trying to explain the delayed
535 gamma-ray and radio response in Mrk 421 by an adiabatic ex-
536 pansion of the blob. The adiabatic expansion of the blob is ex-
537 pected to induce a decrease in the electron density on timescales
538 of $T_{ad}(t) = \frac{R(t)}{3\beta_{exp}c}$ ([Gould 1975](#)). At the time of the VHE flares
539 $R \sim 10^{15} \text{ cm}$, hence $T_{ad} \approx 3 \times 10^2 \text{ hrs}$, corresponding to $\approx 10 \text{ hrs}$
540 in the observers frame, being much longer than the minimum
541 variability timescale noted at VHE (22 min). Hence, the VHE
542 flux variability at the shortest timescales is likely dominantly
543 driven by acceleration and cooling mechanisms and negligibly
544 affected by the expansion of the blob. 545

546 6.2. Multiband correlations as a probe of SSC in the jet

547 We find a close correlation between the emission in the VHE
548 gamma rays at zero time delay and the X-rays over an order
549 of magnitude in flux. We also find a comparable level of vari-
550 ability in both energy bands, similar to the results in [MAGIC
Collaboration et al. \(2021\)](#) and [Acciari et al. \(2021\)](#). The tight
551 correlation and similar variability behavior suggest a cospatial
552 origin, which is in good agreement with the SSC scenario (e.g.
553 [Maraschi et al. 1992](#)). The strongest correlation is found between
554 the 0.3-2 keV and >200 GeV bands reaching a level of 4σ . As-
555 suming standard values for the jet parameters ($B = 0.1 \text{ G}$ and
556 $\delta = 35$ (see e.g. [Aleksić et al. 2015c](#))), one derives that elec-
557 trons with Lorentz factor of around 10^5 (source reference frame)
558 are required to emit $\sim \text{keV}$ photons (in observer's frame). Using
559 Eq. 14 of [Tavecchio et al. \(1998\)](#), which takes into account the
560 Klein-Nishina effects, one expects that electrons with such en-
561 ergy would emit $\sim 0.5 \text{ TeV}$ photons via IC scattering of $\sim \text{keV}$
562 photons. This is well in agreement with the correlation trends. 563

564 We also report marginally significant correlations between
565 the UV and HE gamma rays for the first time in Mrk 421, with
566 both bands showing a similar degree of variability. The pattern is
567 again consistent with the SSC model, but in this case caused by

568 electrons of lower energies populating a larger emission zone.
 569 Following an analogous approach as in the previous case, we
 570 derive estimates of the necessary electron Lorentz factors. Syn-
 571 chrotron photons in the UV W1 band are produced by electrons
 572 with a Lorentz factor of $\sim 10^4$. These electrons produce IC emis-
 573 sion at a few tens of GeV, falling well within the 3-300 GeV
 574 band, for which the highest correlation is observed.

575 The correlation strength decreases to a non-significant level
 576 when going from the UV to the optical band. Even though the
 577 UV and R-band are close together in frequency, these results im-
 578 ply that the underlying particle population responsible for the HE
 579 gamma rays are dominantly radiating in the UV rather than in
 580 the R-band (assuming a leptonic model). Carnerero et al. (2017)
 581 and Acciari et al. (2021) reported significant positive correla-
 582 tions between the HE gamma rays and the R-band. These two
 583 studies considered much longer periods (~ 8 years) where, in re-
 584 lative terms, Mrk 421 showed overall lower activity. The slightly
 585 different correlation behavior might be explained by the different
 586 overall magnitude and timescales of the flux variability consid-
 587 ered, as well as the underlying mechanisms driving the emission
 588 variability (such as the evolution of the emitting region environ-
 589 ment, change in the acceleration and cooling efficiencies etc...)

590 6.3. Evidence of multiple emission zones

591 We find no correlation between the X-ray and the UV. The most
 592 simple explanation of this result is with the existence of two sep-
 593 arate particle populations, of which a compact zone with higher
 594 particle energies is responsible for the keV (and TeV) emission,
 595 and a larger and more extended zone dominates the emission in
 596 the eV (and possibly GeV) band. If the compact zone is em-
 597 bedded into the larger zone, this two-zone scenario would also
 598 be consistent with the marginal significant ($\sim 2.0 - 2.3 \sigma$) cor-
 599 relation between VHE gamma rays and the UV. Should the UV
 600 emission increase due to a change in the underlying particle pop-
 601 ulation, synchrotron photons from the extended zone would en-
 602 ter the compact zone and provide additional seed photons, which
 603 would then be IC scattered and hence produce an increase in the
 604 observed VHE gamma-ray flux.

605 The preference for a multiple-zone scenario was also noted
 606 in earlier works that included X-ray data from this campaign (see
 607 e.g. Kapanadze et al. 2018). It is also further motivated by new
 608 findings of the Imaging X-ray Polarimetry Explorer (*IXPE*),
 609 which suggest an energy dependency of the polarization degree
 610 from radio to the X-ray. The energy dependency points towards
 611 an energy-stratified jet creating emission zones of different ex-
 612 tent (Di Gesu et al. 2022, 2023; Abe et al. 2023). The proposed
 613 scenario of two separate emission zones is a simplified imple-
 614 mentation of an energy-stratified jet. Similar polarization results
 615 have also been found for the HSP Mrk 501 (Liodakis et al. 2022).
 616 The outlined two-zone leptonic model with interaction between
 617 the zones has been successfully used to fit the SEDs during the
 618 *IXPE* observations (Abe et al. 2024).

619 6.4. Peculiarities of the exceptional flare in February 2010

620 We find a positive correlation between the VHE and HE gamma
 621 rays over the whole campaign. A similar correlation was first re-
 622 ported for a dataset taken in 2015-2016, during which Mrk 421
 623 was in a historically low-activity state (Acciari et al. 2021). How-
 624 ever, the correlation in our data set is non-significant when re-
 625 moving the 3-day interval related to the large February 2010
 626 flare, and hence these two bands were directly connected only

during this exceptional flaring event. In other words, the VHE
 versus HE correlation is not representative of the behavior of
 Mrk 421 during the 8-month long 2010 campaign (which covers
 different activity levels).

The same phenomenon is observed when considering the
 HE gamma rays and the X-rays, for which the correlation also
 becomes non-significant when the 3-day time interval of the
 February 2010 flare is removed. Including the flare, we find the
 strongest correlation for the highest-energy band of *Fermi*-LAT
 (3-300 GeV) and the lowest-energy band of *Swift*-XRT (0.3-
 2 keV). While our study shows that the X-ray and VHE radi-
 ation share a common emission region and the UV and HE bands
 may originate from a different region, the flare could be driven
 by a single compact zone whose activity is so high that it not
 only dominates in the VHE radiation, but also contributes sig-
 nificantly to the emission of HE gamma rays on these days. The
 X-ray and HE gamma-ray bands might then be close to the peak
 of the SED bumps caused by synchrotron and IC emission of
 the same particles. Matching this scenario, the 0.3-3 GeV band,
 sitting at the rising edge of the second bump, and the 2-10 keV
 band, sitting at the falling edge of the synchrotron bump, show
 the weakest correlation.

Acknowledgements. Author contribution: J. Abhir: MAGIC analysis cross-
 check; A. Arbet-Engels: variability and correlation analysis, discussion and
 interpretation, paper drafting; D. Paneque: coordination of MWL observations
 and coordination of the MWL data reduction, *RXTE*-PCA analysis, discussion
 and interpretation, paper drafting; F. Schmuckermaier: project management,
 MAGIC and *Fermi*-LAT data analysis, variability and correlation analysis,
 discussion and interpretation, paper drafting; The rest of the authors have
 contributed in one or several of the following ways: design, construction,
 maintenance and operation of the instrument(s) used to acquire the data;
 preparation and/or evaluation of the observation proposals; data acquisition,
 processing, calibration and/or reduction; production of analysis tools and/or
 related Monte Carlo simulations; overall discussions about the contents of the
 draft, as well as related refinements in the descriptions.

The MAGIC collaboration would like to thank the Instituto de Astrofísica
 de Canarias for the excellent working conditions at the Observatorio
 del Roque de los Muchachos in La Palma. The financial support of
 the German BMBF, MPG and HGF; the Italian INFN and INAF; the
 Swiss National Fund SNF; the grants PID2019-104114RB-C31, PID2019-
 104114RB-C32, PID2019-104114RB-C33, PID2019-105510GB-C31,
 PID2019-107847RB-C41, PID2019-107847RB-C42, PID2019-107847RB-
 C44, PID2019-107988GB-C22, PID2022-136828NB-C41, PID2022-
 137810NB-C22, PID2022-138172NB-C41, PID2022-138172NB-C42,
 PID2022-138172NB-C43, PID2022-139117NB-C41, PID2022-139117NB-
 C42, PID2022-139117NB-C43, PID2022-139117NB-C44 funded by the
 Spanish MCIN/AEI/ 10.13039/501100011033 and “ERDF A way of making
 Europe”; the Indian Department of Atomic Energy; the Japanese ICRR, the
 University of Tokyo, JSPS, and MEXT; the Bulgarian Ministry of Education and
 Science, National RI Roadmap Project DOI-400/18.12.2020 and the Academy
 of Finland grant nr. 320045 is gratefully acknowledged. This work was also
 been supported by Centros de Excelencia “Severo Ochoa” y Unidades “María
 de Maeztu” program of the Spanish MCIN/AEI/ 10.13039/501100011033
 (CEX2019-000920-S, CEX2019-000918-M, CEX2021-001131-S) and by the
 CERCA institution and grants 2021SGR00426 and 2021SGR00773 of the
 Generalitat de Catalunya; by the Croatian Science Foundation (HrZZ) Project
 IP-2022-10-4595 and the University of Rijeka Project uniri-prirod-18-48; by
 the Deutsche Forschungsgemeinschaft (SFB1491) and by the Lamarr-Institute
 for Machine Learning and Artificial Intelligence; by the Polish Ministry Of
 Education and Science grant No. 2021/WK/08; and by the Brazilian MCTIC,
 CNPq and FAPERJ.

The *Fermi* LAT Collaboration acknowledges generous ongoing support from
 a number of agencies and institutes that have supported both the development
 and the operation of the LAT as well as scientific data analysis. These include
 the National Aeronautics and Space Administration and the Department of
 Energy in the United States, the Commissariat à l’Energie Atomique and the
 Centre National de la Recherche Scientifique / Institut National de Physique
 Nucléaire et de Physique des Particules in France, the Agenzia Spaziale Italiana
 and the Istituto Nazionale di Fisica Nucleare in Italy, the Ministry of Education,
 Culture, Sports, Science and Technology (MEXT), High Energy Accelerator
 Research Organization (KEK) and Japan Aerospace Exploration Agency
 (JAXA) in Japan, and the K. A. Wallenberg Foundation, the Swedish Research
 Council and the Swedish National Space Board in Sweden. Additional support

700 for science analysis during the operations phase is gratefully acknowledged
 701 from the Istituto Nazionale di Astrofisica in Italy and the Centre National
 702 d'Études Spatiales in France. This work performed in part under DOE
 703 Contract DE-AC02-76SF00515. A.A.E. and D.P. acknowledge support from the
 704 Deutsche Forschungsgemeinschaft (DFG; German Research Foundation) under
 705 Germany's Excellence Strategy EXC-2094-390783311.
 706 The research at Boston University was supported in part by several NASA
 707 Fermi Guest Investigator grants, the latest of which are 80NSSC23K1507 and
 708 80NSSC23K1508. This study was based in part on observations conducted using
 709 the 1.8m Perkins Telescope Observatory (PTO) in Arizona, which is owned
 710 and operated by Boston University. The VLBA is an instrument of the National
 711 Radio Astronomy Observatory. The National Radio Astronomy Observatory is a
 712 facility of the National Science Foundation operated by Associated Universities,
 713 Inc. Research at UMRAO was supported by a series of grants from the NSF
 714 (most recently AST-0607523) and from NASA (including Fermi G.I. awards
 715 NNX09AU16G, NNX10API6G, NNX11AO13G, and NNX13AP18G). Funds for
 716 the operation of UMRAO were provided by the University of Michigan. The
 717 Submillimeter Array is a joint project between the Smithsonian Astrophysical
 718 Observatory and the Academia Sinica Institute of Astronomy and Astrophysics
 719 and is funded by the Smithsonian Institution and the Academia Sinica. We
 720 recognize that Maunakea is a culturally important site for the indigenous
 721 Hawaiian people; we are privileged to study the cosmos from its summit.

722 References

723 Abdo, A. A., Ackermann, M., Agudo, I., et al. 2010a, *ApJ*, 716, 30
 724 Abdo, A. A., Ackermann, M., Ajello, M., et al. 2010b, *ApJ*, 722, 520
 725 Abdo, A. A., Ackermann, M., Ajello, M., et al. 2011, *ApJ*, 736, 131
 726 Abdollahi, S., Acero, F., Ackermann, M., et al. 2020, *ApJS*, 247, 33
 727 Abe, S., Abhir, J., Acciari, V. A., et al. 2024, Insights into the broad-band emis-
 728 sion of the TeV blazar Mrk 501 during the first X-ray polarization measure-
 729 ments
 730 Abe, S., Abhir, J., Acciari, V. A., et al. 2023, First characterization of the emis-
 731 sion behavior of Mrk421 from radio to VHE gamma rays with simultaneous
 732 X-ray polarization measurements
 733 Abeyssekara, A. U., Benbow, W., Bird, R., et al. 2020, *ApJ*, 890, 97
 734 Acciari, V. A., Ansoldi, S., Antonelli, L. A., et al. 2020, *ApJS*, 248, 29
 735 Acciari, V. A., Ansoldi, S., Antonelli, L. A., et al. 2021, *MNRAS*, 504, 1427
 736 Acciari, V. A., Arlen, T., Aune, T., et al. 2014, *Astroparticle Physics*, 54, 1
 737 Ackermann, M., Ajello, M., Albert, A., et al. 2012, *ApJS*, 203, 4
 738 Ahnen, M. L., Ansoldi, S., Antonelli, L. A., et al. 2017, *Astroparticle Physics*,
 739 94, 29
 740 Ajello, M., Baldini, L., Ballet, J., et al. 2022, *ApJS*, 263, 24
 741 Aleksić, J., Ansoldi, S., Antonelli, L. A., et al. 2015a, *A&A*, 573, A50
 742 Aleksić, J., Ansoldi, S., Antonelli, L. A., et al. 2015b, *A&A*, 576, A126
 743 Aleksić, J., Ansoldi, S., Antonelli, L. A., et al. 2015c, *A&A*, 578, A22
 744 Aleksić, J., Ansoldi, S., Antonelli, L. A., et al. 2016, *Astroparticle Physics*, 72,
 745 76
 746 Arbet Engels, A. 2021, Doctoral thesis, ETH Zurich, Zurich
 747 Atwood, W. B., Abdo, A. A., Ackermann, M., et al. 2009, *ApJ*, 697, 1071
 748 Baloković, M., Paneque, D., Madejski, G., et al. 2016, *ApJ*, 819, 156
 749 Blasi, M. G., Lico, R., Giroletti, M., et al. 2013, *A&A*, 559, A75
 750 Bradt, H. V., Rothschild, R. E., & Swank, J. H. 1993, *A&AS*, 97, 355
 751 Breeveld, A. A., Landsman, W., Holland, S. T., et al. 2011, in *American Institute*
 752 *of Physics Conference Series*, Vol. 1358, *Gamma Ray Bursts 2010*, ed. J. E.
 753 McEnery, J. L. Racusin, & N. Gehrels, 373–376
 754 Burrows, D. N., Hill, J. E., Nousek, J. A., et al. 2005, *Space Sci. Rev.*, 120, 165
 755 Carnerero, M. I., Raiteri, C. M., Villata, M., et al. 2017, *MNRAS*, 472, 3789
 756 Cerruti, M., Zech, A., Boisson, C., & Inoue, S. 2015, *MNRAS*, 448, 910
 757 Chatterjee, R., Jorstad, S. G., Marscher, A. P., et al. 2008, *ApJ*, 689, 79
 758 Dermer, C. D., Schlickeiser, R., & Mastichiadis, A. 1992, *A&A*, 256, L27
 759 Di Gesu, L., Donnarumma, I., Tavecchio, F., et al. 2022, *ApJ*, 938, L7
 760 Di Gesu, L., Marshall, H. L., Ehlert, S. R., et al. 2023, *Nature Astronomy*, 7,
 761 1245
 762 Dondi, L. & Ghisellini, G. 1995, *MNRAS*, 273, 583
 763 Edelson, R. A. & Krolik, J. H. 1988, *ApJ*, 333, 646
 764 Emmanoulopoulos, D., McHardy, I. M., & Papadakis, I. E. 2013, *MNRAS*, 433,
 765 907
 766 Fitzpatrick, E. L. 1999, *PASP*, 111, 63
 767 Fossati, G., Buckley, J. H., Bond, I. H., et al. 2008, *ApJ*, 677, 906
 768 Gaidos, J. A., Akerlof, C. W., Biller, S., et al. 1996, *Nature*, 383, 319
 769 Georganopoulos, M. & Kazanas, D. 2003, *ApJ*, 594, L27
 770 Ghisellini, G., Celotti, A., Fossati, G., Maraschi, L., & Comastri, A. 1998, *MN-*
 771 *RAS*, 301, 451
 772 Ghisellini, G., Tavecchio, F., & Chiaberge, M. 2005, *A&A*, 432, 401
 773 Gould, R. J. 1975, *ApJ*, 196, 689
 774 Hovatta, T., Petropoulou, M., Richards, J. L., et al. 2015, *MNRAS*, 448, 3121

Jormanainen, J., Hovatta, T., Christie, I. M., et al. 2023, *A&A*, 678, A140
 Jorstad, S. G., Marscher, A. P., Mattox, J. R., et al. 2001, *ApJ*, 556, 738
 Jorstad, S. G., Marscher, A. P., Morozova, D. A., et al. 2017, *ApJ*, 846, 98
 Kapanadze, B., Vercellone, S., Romano, P., et al. 2018, *ApJ*, 858, 68
 Kastendieck, M. A., Ashley, M. C. B., & Horns, D. 2011, *A&A*, 531, A123
 Lico, R., Giroletti, M., Orienti, M., et al. 2012, *A&A*, 545, A117
 Liodakis, I., Marscher, A. P., Agudo, I., et al. 2022, *Nature*, 611, 677
 Lomb, N. R. 1976, *Ap&SS*, 39, 447
 Madejski, G. M., Sikora, M., Jaffe, T., et al. 1999, *ApJ*, 521, 145
 MAGIC Collaboration. 2020, *Astronomy & Astrophysics*, 635, A158
 MAGIC Collaboration, Acciari, V. A., Ansoldi, S., et al. 2017, *A&A*, 655, A89
 MAGIC Collaboration, Ahnen, M. L., Ansoldi, S., et al. 2018, *A&A*, 619, A45
 Mannheim, K. 1993, *A&A*, 269, 67
 Maraschi, L., Ghisellini, G., & Celotti, A. 1992, *ApJ*, 397, L5
 Marscher, A. P., Jorstad, S. G., D'Arcangelo, F. D., et al. 2008, *Nature*, 452, 966
 Max-Moerbeck, W., Richards, J. L., Hovatta, T., et al. 2014, *MNRAS*, 445, 437
 Mücke, A. & Protheroe, R. J. 2001, *Astroparticle Physics*, 15, 121
 Padovani, P., Alexander, D. M., Assef, R. J., et al. 2017, *A&A Rev.*, 25, 2
 Peterson, B. M., Wanders, I., Horne, K., et al. 1998, *PASP*, 110, 660
 Piner, B. G. & Edwards, P. G. 2005, *ApJ*, 622, 168
 Poutanen, J., Zdziarski, A. A., & Ibragimov, A. 2008, *MNRAS*, 389, 1427
 Richards, J. L., Hovatta, T., Lister, M. L., et al. 2013, in *European Physical Jour-*
 796 *nal Web of Conferences*, Vol. 61, *European Physical Journal Web of Confer-*
 797 *ences*, 04010
 Roming, P. W. A., Kennedy, T. E., Mason, K. O., et al. 2005, *Space Sci. Rev.*,
 800 120, 95
 Scargle, J. D. 1982, *ApJ*, 263, 835
 Schlaflly, E. F. & Finkbeiner, D. P. 2011, *ApJ*, 737, 103
 Schlegel, D. J., Finkbeiner, D. P., & Davis, M. 1998, *ApJ*, 500, 525
 Sikora, M., Begelman, M. C., & Rees, M. J. 1994, *ApJ*, 421, 153
 Tavecchio, F., Maraschi, L., & Ghisellini, G. 1998, *ApJ*, 509, 608
 Tramacere, A., Sliusar, V., Walter, R., Jurysek, J., & Balbo, M. 2022, *A&A*, 658,
 806 A173
 Urry, C. M. & Padovani, P. 1995, *PASP*, 107, 803
 Uttley, P., McHardy, I. M., & Papadakis, I. E. 2002, *MNRAS*, 332, 231
 Vaughan, S., Edelson, R., Warwick, R. S., & Uttley, P. 2003, *MNRAS*, 345, 1271
 Villata, M., Raiteri, C. M., Gurwell, M. A., et al. 2009, *A&A*, 504, L9
 Villata, M., Raiteri, C. M., Larionov, V. M., et al. 2008, *A&A*, 481, L79
 Weaver, Z. R., Jorstad, S. G., Marscher, A. P., et al. 2022, *ApJS*, 260, 12
 Welsh, W. F. 1999, *PASP*, 111, 1347
 Zanin, R., Carmona, E., Sitarek, J., et al. 2013, in *International Cosmic Ray*
 815 *Conference*, Vol. 33, *International Cosmic Ray Conference*, 2937
 816

1 Japanese MAGIC Group: Department of Physics, Tokai University, 817
 Hiratsuka, 259-1292 Kanagawa, Japan 818
 2 Japanese MAGIC Group: Institute for Cosmic Ray Research 819
 (ICRR), The University of Tokyo, Kashiwa, 277-8582 Chiba, Japan 820
 3 ETH Zürich, CH-8093 Zürich, Switzerland 821
 4 Università di Siena and INFN Pisa, I-53100 Siena, Italy 822
 5 Institut de Física d'Altes Energies (IFAE), The Barcelona Institute 823
 of Science and Technology (BIST), E-08193 Bellaterra (Barcelona), 824
 Spain 825
 6 Universitat de Barcelona, ICCUB, IEEC-UB, E-08028 Barcelona, 826
 Spain 827
 7 Instituto de Astrofísica de Andalucía-CSIC, Glorieta de la As- 828
 tronómia s/n, 18008, Granada, Spain 829
 8 National Institute for Astrophysics (INAF), I-00136 Rome, Italy 830
 9 Università di Udine and INFN Trieste, I-33100 Udine, Italy 831
 10 Max-Planck-Institut für Physik, D-85748 Garching, Germany 832
 11 Università di Padova and INFN, I-35131 Padova, Italy 833
 12 Technische Universität Dortmund, D-44221 Dortmund, Germany 834
 13 Croatian MAGIC Group: University of Zagreb, Faculty of Electrical 835
 Engineering and Computing (FER), 10000 Zagreb, Croatia 836
 14 Centro Brasileiro de Pesquisas Físicas (CBPF), 22290-180 URCA, 837
 Rio de Janeiro (RJ), Brazil 838
 15 IPARCOS Institute and EMFTEL Department, Universidad Complu- 839
 tense de Madrid, E-28040 Madrid, Spain 840
 16 Instituto de Astrofísica de Canarias and Dpto. de Astrofísica, Uni- 841
 versidad de La Laguna, E-38200, La Laguna, Tenerife, Spain 842
 17 University of Lodz, Faculty of Physics and Applied Informatics, De- 843
 partment of Astrophysics, 90-236 Lodz, Poland 844
 18 Centro de Investigaciones Energéticas, Medioambientales y Tec- 845
 nológicas, E-28040 Madrid, Spain 846

847	¹⁹ Departament de Física, and CERES-IEEC, Universitat Autònoma de	⁵³ Department of Astronomy, University of Michigan, 323 West Hall,	916
848	Barcelona, E-08193 Bellaterra, Spain	1085 S. University Avenue, Ann Arbor Michigan 48109, USA	917
849	²⁰ Università di Pisa and INFN Pisa, I-56126 Pisa, Italy	⁵⁴ Departamento de Astronomía, Universidad de Chile, Camino El Ob-	918
850	²¹ INFN MAGIC Group: INFN Sezione di Bari and Dipartimento In-	servatorio 1515, Las Condes, Santiago, Chile	919
851	terateneo di Fisica dell'Università e del Politecnico di Bari, I-70125	⁵⁵ Institute of Astrophysics, Foundation for Research and Technology	920
852	Bari, Italy	– Hellas, 100 Nikolaou Plastira str. Vassilika Vouton, 70013 Herak-	921
853	²² Department for Physics and Technology, University of Bergen, Nor-	lion, Crete, Greece	922
854	way	⁵⁶ Owens Valley Radio Observatory, California Institute of Technol-	923
855	²³ INFN MAGIC Group: INFN Sezione di Torino and Università degli	ogy, Pasadena, CA91125, US	924
856	Studi di Torino, I-10125 Torino, Italy	⁵⁷ Aalto University Metsähovi Radio Observatory, Metsähovintie 114,	925
857	²⁴ Croatian MAGIC Group: University of Rijeka, Faculty of Physics,	02540 Kylmäla, Finland	926
858	51000 Rijeka, Croatia	⁵⁸ Aalto University Department of Electronics and Nanoengineering,	927
859	²⁵ Universität Würzburg, D-97074 Würzburg, Germany	P.O. BOX 15500, FI-00076 AALTO, Finland	928
860	²⁶ Japanese MAGIC Group: Physics Program, Graduate School of Ad-	⁵⁹ Center for Astrophysics Harvard & Smithsonian, 60 Garden Street,	929
861	vanced Science and Engineering, Hiroshima University, 739-8526	Cambridge, MA 02138 USA	930
862	Hiroshima, Japan	⁶⁰ Space Science Institute, 4765 Walnut St., Suite B, Boulder, CO	931
863	²⁷ Deutsches Elektronen-Synchrotron (DESY), D-15738 Zeuthen,	80301, USA	932
864	Germany		
865	²⁸ Armenian MAGIC Group: ICRA Net-Armenia, 0019 Yerevan, Ar-		
866	menia		
867	²⁹ Croatian MAGIC Group: University of Split, Faculty of Electri-		
868	cal Engineering, Mechanical Engineering and Naval Architecture		
869	(FESB), 21000 Split, Croatia		
870	³⁰ Croatian MAGIC Group: Josip Juraj Strossmayer University of Os-		
871	ijek, Department of Physics, 31000 Osijek, Croatia		
872	³¹ Finnish MAGIC Group: Finnish Centre for Astronomy with ESO,		
873	Department of Physics and Astronomy, University of Turku, FI-		
874	20014 Turku, Finland		
875	³² Saha Institute of Nuclear Physics, A CI of Homi Bhabha National		
876	Institute, Kolkata 700064, West Bengal, India		
877	³³ Inst. for Nucl. Research and Nucl. Energy, Bulgarian Academy of		
878	Sciences, BG-1784 Sofia, Bulgaria		
879	³⁴ Japanese MAGIC Group: Department of Physics, Yamagata Univer-		
880	sity, Yamagata 990-8560, Japan		
881	³⁵ Finnish MAGIC Group: Space Physics and Astronomy Research		
882	Unit, University of Oulu, FI-90014 Oulu, Finland		
883	³⁶ Japanese MAGIC Group: Chiba University, ICEHAP, 263-8522		
884	Chiba, Japan		
885	³⁷ Japanese MAGIC Group: Institute for Space-Earth Environmental		
886	Research and Kobayashi-Maskawa Institute for the Origin of Parti-		
887	cles and the Universe, Nagoya University, 464-6801 Nagoya, Japan		
888	³⁸ Japanese MAGIC Group: Department of Physics, Kyoto University,		
889	606-8502 Kyoto, Japan		
890	³⁹ INFN MAGIC Group: INFN Roma Tor Vergata, I-00133 Roma,		
891	Italy		
892	⁴⁰ University of Geneva, Chemin d'Ecogia 16, CH-1290 Versoix,		
893	Switzerland		
894	⁴¹ Japanese MAGIC Group: Department of Physics, Konan University,		
895	Kobe, Hyogo 658-8501, Japan		
896	⁴² also at International Center for Relativistic Astrophysics (ICRA),		
897	Rome, Italy		
898	⁴³ also at Port d'Informació Científica (PIC), E-08193 Bellaterra		
899	(Barcelona), Spain		
900	⁴⁴ also at Department of Physics, University of Oslo, Norway		
901	⁴⁵ also at Dipartimento di Fisica, Università di Trieste, I-34127 Trieste,		
902	Italy		
903	⁴⁶ also at INAF Padova		
904	⁴⁷ Japanese MAGIC Group: Institute for Cosmic Ray Research		
905	(ICRR), The University of Tokyo, Kashiwa, 277-8582 Chiba, Japan		
906	⁴⁸ INAF Istituto di Radioastronomia, Via P. Gobetti 101, I-40129		
907	Bologna, Italy		
908	⁴⁹ Institute for Astrophysical Research, Boston University, 725 Com-		
909	monwealth Avenue, Boston, MA 02215, USA		
910	⁵⁰ Space Science Data Center, Agenzia Spaziale Italiana, Via del Po-		
911	litecnico snc, 00133 Roma, Italy		
912	⁵¹ INAF Osservatorio Astronomico di Roma, Via Frascati 33, 00078		
913	Monte Porzio Catone (RM), Italy		
914	⁵² ASI - Agenzia Spaziale Italiana, Via del Politecnico snc, 00133		
915	Roma, Italy		

933 Appendix A: Observations and data processing

934 This section contains a detailed description of all used instru- 988
935 ments and their corresponding data analysis. Since the same 989
936 campaign is exploited in parts in [Aleksić et al. \(2015c\)](#), some in- 990
937 strument sections closely follow the descriptions given in there. 991

938 Appendix A.1: VHE gamma rays

939 The MAGIC telescopes are two Imaging Atmospheric 992
940 Cherenkov Telescopes (IACTs), MAGIC I and MAGIC II, 993
941 each with a diameter of 17 m, located at Observatorio del 994
942 Roque de los Muchachos (ORM, 28.762°N 17.890°W, 2200 995
943 m above sea level) on the Canary Island of La Palma. With 996
944 the start of stereoscopic observations in 2009 and substantial 997
945 hardware upgrades completed in 2012, MAGIC is capable of 998
946 detecting gamma rays with energies from about 30 GeV up to 999
947 $\gtrsim 100$ TeV ([Aleksić et al. 2016](#); [MAGIC Collaboration 2020](#)). 1000

948 This work covers the time period from November 11, 2009, 1001
949 (MJD 55149) until June 16, 2010, (MJD 55363). In total, the 1002
950 MAGIC telescopes observed Mrk 421 for 62.4 h in the zenith 1003
951 angle range between 5° and 50°. The data are analyzed using the 1004
952 MAGIC Analysis and Reconstruction Software, MARS ([Zanin 1005
et al. 2013](#); [Aleksić et al. 2016](#)). The final data are selected based 1006
953 on quality criteria to exclude periods with unfavorable weather 1007
954 conditions or too bright moon. The data were taken under low 1008
955 moonlight conditions in order to limit contamination from night 1009
956 sky background light ([Ahnen et al. 2017](#)). After applying quality 1010
957 cuts, 50.1 h of data remained. 1011

958 This work focuses on the MWL variability and correlations, 1012
959 and hence, we use light curves that report the VHE gamma-ray 1013
960 emission of Mrk 421. Due to the high gamma-ray brightness of 1014
961 Mrk 421, we can construct two separate light curves in the VHE 1015
962 band covering two energy ranges: 0.2-1 TeV and >1 TeV. The 1016
963 analysis was performed for the whole campaign including the 1017
964 already published periods in [Aleksić et al. \(2015c\)](#) and [Abey- 1018
sekara et al. \(2020\)](#). This ensures that the low-level analysis re- 1019
965 mains consistent throughout and the results are well compatible. 1020
966 In addition to the data from MAGIC, we also used VERITAS 1021
967 light curves with VHE gamma-ray fluxes above 0.2 TeV pub- 1022
968 lished in [Aleksić et al. \(2015c\)](#) and [Abeysekara et al. \(2020\)](#). In 1023
969 order to create a joint light curve, a third light curve was con- 1024
970 structed from the MAGIC data for this energy range. 1025

973 Appendix A.2: HE gamma rays

974 The *Fermi Gamma-ray Space Telescope* satellite carries the LAT 1026
975 detector on board. It is a pair-conversion telescope surveying the 1027
976 gamma-ray sky in the 20 MeV to > 300 GeV energy range ([At- 1028
wood et al. 2009](#); [Ackermann et al. 2012](#)). For the construction of 1029
977 light curves, we perform a binned-likelihood analysis using tools 1030
978 from the FERMITOOLS software³ v2.2.0. We use the instrument 1031
979 response function P8R3_SOURCE_V3 and the diffuse background 1032
980 models⁴ g11_iem_v07 and iso_P8R3_SOURCE_V3_v1. 1033

981 We create two light curves in the range from 0.3 GeV to 1034
982 3 GeV and 3 GeV to 300 GeV by selecting Source class events 1035
983 in a circular region of interest (ROI) with a radius of 20° around 1036
984 Mrk 421 in the respective energy band. All events with a zenith 1037
985 angle above 90° are discarded to reduce the contribution from 1038
986 limb gamma rays. The analysis threshold energy of 0.3 GeV was 1039

chosen over the more usual 0.1 GeV in order to make use of 988
the improved angular resolution of *Fermi*-LAT at higher ener- 989
gies. A higher energy threshold additionally reduces background 990
contamination, which leads to an overall improvement of the 991
signal-to-noise ratio for hard sources (photon index < 2) such as 992
Mrk 421. For the source model, we include all sources from the 993
fourth *Fermi*-LAT source catalog Data Release 3 (4FGL-DR3; 994
[Abdollahi et al. 2020](#); [Ajello et al. 2022](#)) that are found within 995
the ROI plus an additional 5°. We fit the obtained model to our 996
data covering the time period from November 2, 2009, (MJD 997
55141) to July 2, 2010, (MJD 55379). The initial fit results are 998
used to remove weak components from the model (counts < 1 or 999
TS $< 3^5$). After the first optimization, each time bin is fit with the 1000
model. During the fitting procedure, the normalization of bright 1001
sources (TS > 10), sources close to the ROI center ($< 3^\circ$), the 1002
diffuse background, and the spectral parameters of Mrk 421 it- 1003
self are allowed to vary. We produce the light curves with a 3- 1004
day binning. In all time bins, the source is detected with TS > 25 1005
(i.e., $> 5\sigma$). 1006

Appendix A.3: X-rays

1007 We scheduled observations with the X-Ray Telescope (XRT; 1008
[Burrows et al. 2005](#)) on board the *Neil Gehrels Swift Obser- 1009
vatory (Swift)* throughout the full campaign to achieve the best 1010
possible coincidence with VHE observations. All *Swift*-XRT ob- 1011
servations were carried out both in Windowed Timing (WT) and 1012
Photon Counting (PC) readout modes. The data were then pro- 1013
cessed using the XRTDAS software package (v.3.7.0) developed 1014
by the ASI Space Science Data Center⁶ (SSDC), released by 1015
the NASA High Energy Astrophysics Archive Research Center 1016
(HEASARC) in the HEASoft package (v.6.30.1). The data were 1017
reprocessed with the `xrtpipeline` script and using calibration 1018
files from *Swift*-XRT CALDB (version 20210915). The X-ray 1019
spectrum was constructed from the calibrated and cleaned event 1020
file for each pointing. The events were selected within a radius 1021
of 20 pixels (~ 47 arcsec) in both WT and PC modes. The back- 1022
ground was extracted from a nearby circular region with a radius 1023
of 40 pixels. The ancillary response files were generated with the 1024
`xrtmkarf` task applying the corrections for PSF losses and CCD 1025
defects using the cumulative exposure map. The 0.3 – 10 keV 1026
source spectra were binned using the `grppha` task by requiring 1027
at least 20 counts per energy bin. We used XSPEC with both a 1028
power-law and log-parabola model (with a pivot energy fixed at 1029
1 keV and an added photoelectric absorption component assum- 1030
ing an equivalent hydrogen column density fixed to the Galac- 1031
tic value along the line of sight). In the overall majority of the 1032
observations, the preference for a log-parabola model is statisti- 1033
cally significant (i.e., $> 5\sigma$). The intrinsic fluxes were extracted 1034
in the 0.3-2 keV, and 2-10 keV energy bands. 1035

Data from the *Swift* Burst Alert Telescope (BAT) are publicly 1036
accessible online⁷. In this work, the daily light curve is used from 1037
15-50 keV. 1038

The Rossi X-ray Timing Explorer (*RXTE*; [Bradt et al. 1039
1993](#)) satellite performed almost daily pointing observations of 1040
Mrk 421 during the time period from December 12, 2009, (MJD 1041
55177) to April 29, 2010, (MJD 55315). The data were analyzed 1042

⁵ The test statistic TS is defined as $-2\log(\mathcal{L}_{\max,0}/\mathcal{L}_{\max,1})$, where $\mathcal{L}_{\max,0}$ is the maximum likelihood value for a model without an additional source, the null hypothesis, and $\mathcal{L}_{\max,1}$ is the maximum likelihood value for a model with the additional source at a specified location.

⁶ <https://www.ssdsc.asi.it/>

⁷ <https://swift.gsfc.nasa.gov/results/transients/>

³ <https://fermi.gsfc.nasa.gov/ssc/data/analysis/>

⁴ <http://fermi.gsfc.nasa.gov/ssc/data/access/lat/BackgroundModels.html>

1043 using FTOOLS v6.9 following the settings and procedures rec- 1096
 1044 ommended by the NASA RXTE Guest Observer Facility⁸. We 1097
 1045 produce a light curve from 2-10 keV. For more details on the 1098
 1046 analysis settings see the instrument description given in Aleksić 1099
 1047 et al. (2015c).

1048 Data from the *RXTE* All-Sky Monitor (ASM) are publicly 1099
 1049 accessible online⁹. In this work, the one-day average light curve 1100
 1050 in the energy range from 2-12 keV is used. 1101

1051 Appendix A.4: Ultraviolet

1052 *Swift* also provides coverage in the ultraviolet (UV) band from 1099
 1053 the UV/Optical Telescope (UVOT, Roming et al. 2005). We se- 1100
 1054 lected observations in the W1 (251 nm), M2 (217 nm), and W2 1101
 1055 (188 nm) filters by applying standard quality checks to all obser- 1102
 1056 vations in the chosen time interval, excluding those with unstable 1103
 1057 attitudes or affected by contamination from a nearby starlight (51 1104
 1058 UMa). For each individual observation, we performed photom- 1105
 1059 etry over the total exposures in each filter to extract flux val- 1106
 1060 ues. The same apertures for source counts (the standard with 1107
 1061 5 arcsec radius) and background estimation (mostly three-four 1108
 1062 circles of ~ 16 arcsec radii off the source) were applied to all. 1109
 1063 We performed the photometry extraction with the official soft- 1110
 1064 ware included in the HEASoft 6.23 package, from HEASARC, 1111
 1065 and then applied the official calibrations (Breeveld et al. 2011) 1112
 1066 included in the CALDB release (20201026). As a last step, the 1113
 1067 source fluxes were dereddened according to a mean interstel- 1114
 1068 lar extinction curve (Fitzpatrick 1999) and the mean Galactic 1115
 1069 $E(B - V)$ value of 0.0123 mag (Schlegel et al. 1998; Schlafly & 1116
 1070 Finkbeiner 2011).

1071 Appendix A.5: Optical

1072 Observations in the R-band were performed within the GLAST- 1099
 1073 AGILE Support Program (GASP) of the Whole Earth Blazar 1100
 1074 Telescope (WEBT; e.g. Villata et al. 2008, 2009), including mul- 1101
 1075 tiple optical telescopes around the globe. We use the data pub- 1102
 1076 lished in Carnerero et al. (2017), for which the contribution of 1103
 1077 the host galaxy has been subtracted. 1104

1078 Optical polarization measurements are included from the 1099
 1079 Lowell (Perkins), Crimean, Calar Alto, and Steward observato- 1100
 1080 ries, also taken from Carnerero et al. (2017). The contribution 1101
 1081 of the host galaxy is also taken into account for the polarization 1102
 1082 data. 1103

1083 Appendix A.6: Radio

1084 The radio data were taken with the 14 m Metsähovi Radio Ob- 1099
 1085 servatory at 37 GHz, the 40 m Owens Valley Radio Observatory 1100
 1086 (OVRO) telescope at 15 GHz, and the 26 m University of Michi- 1101
 1087 gan Radio Astronomy Observatory (UMRAO) at 14.5 GHz. Obser- 1102
 1088 vations at 225 GHz (1.3 mm) were performed at the Submil- 1103
 1089 limeter Array (SMA) near the summit of Mauna Kea (Hawaii). 1104
 1090 For more details on the instruments and observations see the de- 1105
 1091 scription given in Aleksić et al. (2015c). 1106

1092 In addition, the Very Long Baseline Array (VLBA) per- 1099
 1093 formed observations at 43 GHz. The data were provided by the 1100
 1094 Boston University blazar group¹⁰ and are part of their monitoring 1101
 1095 program of gamma-ray blazars. We obtained the images of the 1102

1096 parsec-scale jet using the Astronomical Image Processing Sys- 1097
 1098 tem (AIPS) and Difmap software packages (Jorstad et al. 2017). 1099

1098 Appendix B: Fitting the power spectral density 1099

1099 The PSD cannot be directly estimated from real data sets. Real 1099
 1100 observations suffer from unevenly sampled data with large gaps 1100
 1101 in the coverage. The limited time coverage as well as the tempo- 1101
 1102 ral binning of the data can cause a transfer of variability power 1102
 1103 from lower to higher frequencies and vice versa. These distor- 1103
 1104 tions need to be accounted for obtaining an accurate estimate of 1104
 1105 the true PSD. 1105

1106 We estimate the true PSD index using a simulation-based 1106
 1107 forward-folding procedure, using the code described in Ar- 1107
 1108 bet Engels (2021); MAGIC Collaboration et al. (2021). We cover 1108
 1109 the parameter space from 0.3 to 2.5 using steps of 0.1. For each 1109
 1110 assumed spectral index, we simulate a set of 3000 light curves 1110
 1111 using the assumption of a power-law-shaped PSD. We use the 1111
 1112 underlying probability distribution described in Emmanoulopou- 1112
 1113 los et al. (2013) to match the observed flux distribution as well 1113
 1114 as possible. We simulate light curves 10 times longer than the 1114
 1115 real light curves and apply the same temporal binning to account 1115
 1116 for the previously mentioned leakage effects. In order to com- 1116
 1117 pare the simulated with the real light curves, we use the multiple 1117
 1118 fractions variance function (MFVF) as a proxy for the PSD (Kas- 1118
 1119 tendieck et al. 2011). The MFVF is computed by splitting a given 1119
 1120 light curve in the temporal middle and taking the flux variance of 1120
 1121 both halves. The two halves are then split again into two, and the 1121
 1122 variances are estimated. This is repeated until a minimum time 1122
 1123 scale of one day is reached (which is the minimum temporal res- 1123
 1124 olution of the light curves). The resulting variances as a function 1124
 1125 of time scale give a robust alternative representation of the PSD. 1125
 1126 The MFVF is computed for all simulated light curves, which re- 1126
 1127 sults in a probability density function $p(a, f_i)$ for each out of N 1127
 1128 frequency bins. It gives the probability of measuring a MFVF 1128
 1129 in the frequency bin f_i , assuming the underlying PSD with the 1129
 1130 index a . The best-fit value for the spectral index of the real light 1130
 1131 curve can then be estimated with a maximum likelihood estima- 1131
 1132 tion by finding the index a maximizing 1132

$$1133 \mathcal{L}(a) = \sum_{i=0}^N \ln(p(a, f_i)). \quad (B.1) \quad 1134$$

1135 Fig. B.1 shows an example likelihood profile for the 2-10 keV 1133
 1136 band. The resulting values for a selected set of light curves are 1134
 1137 given in Tab. 3. 1135

1136 Following Arbet Engels (2021); MAGIC Collaboration et al. 1136
 1137 (2021) we estimated the uncertainties of the indices by simulat- 1137
 1138 ing 100 light curves using the best-fit index for each light curve 1138
 1139 and then refit all 100 created light curves with the same method. 1139
 1140 This creates a histogram of the resulting indices, where the un- 1140
 1141 certainties are given by the 68% (1σ) containment region. As an 1141
 1142 example, Fig. B.2 shows the resulting histogram for the 2-10 keV 1142
 1143 band. Since the histograms can show a skewed distribution, we 1143
 1144 separately provide upper and lower uncertainties. 1144

1145 Appendix C: Intranight VHE variability 1146

1146 Fig. C.1 shows the intranight light curves in the 0.2-1 TeV band 1146
 1147 of four selected nights in 10 min bins. The upper panel shows 1147
 1148 the January 14, 2010, (MJD 55210) light curve, where the high- 1148
 1149 est fluxes are recorded by MAGIC during the flare in January. 1149
 1150 We fit the data with a constant model in order to test the hypoth- 1150
 1151 esis of a non-variable emission. The source shows no significant 1151

⁸ https://heasarc.gsfc.nasa.gov/docs/xte/xhp_proc_analysis.html

⁹ <http://xte.mit.edu/asmlc/ASM.html>

¹⁰ <https://www.bu.edu/blazars/VLBAproject.html>

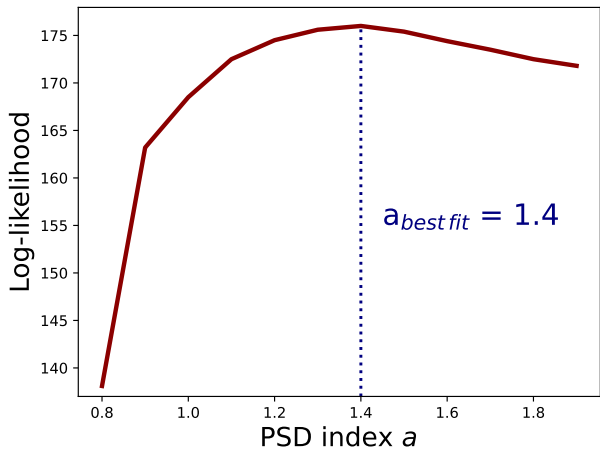


Fig. B.1: Likelihood profile $\mathcal{L}(a)$ (see Eq. B.1) for the 2-10 keV band with its best fit value of 1.4 denoted by a vertical blue dotted line.

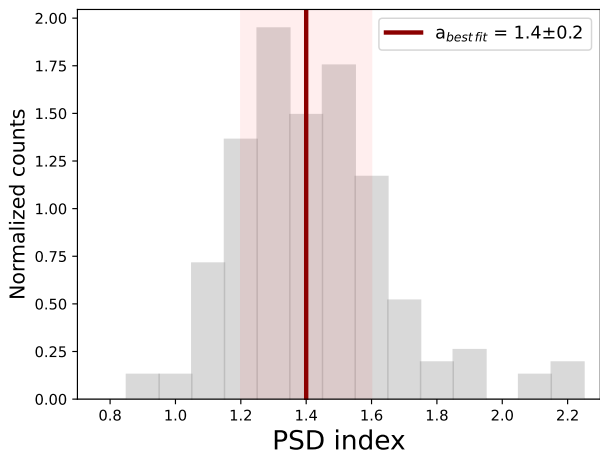


Fig. B.2: Histogram of the best-fit indices derived from simulations using as input a simulated light curve that has a known PSD index $a = 1.4$, in agreement with the real data for the 2-10 keV band.

1152 variability but a stable and high emission throughout the full ex-
1153 posure of around 3 hours.

1154 In the second panel, the following night of January 15 (MJD
1155 55211) is shown. The hypothesis of a constant emission is re-
1156 jected at 3.7σ , indicating a significant variability on a time-scale
1157 of well below 1 hour in VHE gamma rays. Missing data points
1158 in between were caused by technical interruptions.

1159 During the flare in January, the VHE flux increases again
1160 around January 20 (MJD 55216). We see no significant vari-
1161 ability but again a strong but constant emission throughout the
1162 exposure.

1163 Lastly, we show April 18 (MJD 55304) in the lowest panel.
1164 We observe a quick decay and small rise of the flux, which cor-
1165 responds to significant variability at 4.5σ .

1166 Appendix D: Hardness ratios of VHE gamma rays 1167 and X-rays

1168 Fig. D.1 shows the hardness ratios (HR) of all MAGIC obser-
1169 vations as a function of the flux between 0.2-1 TeV in the left

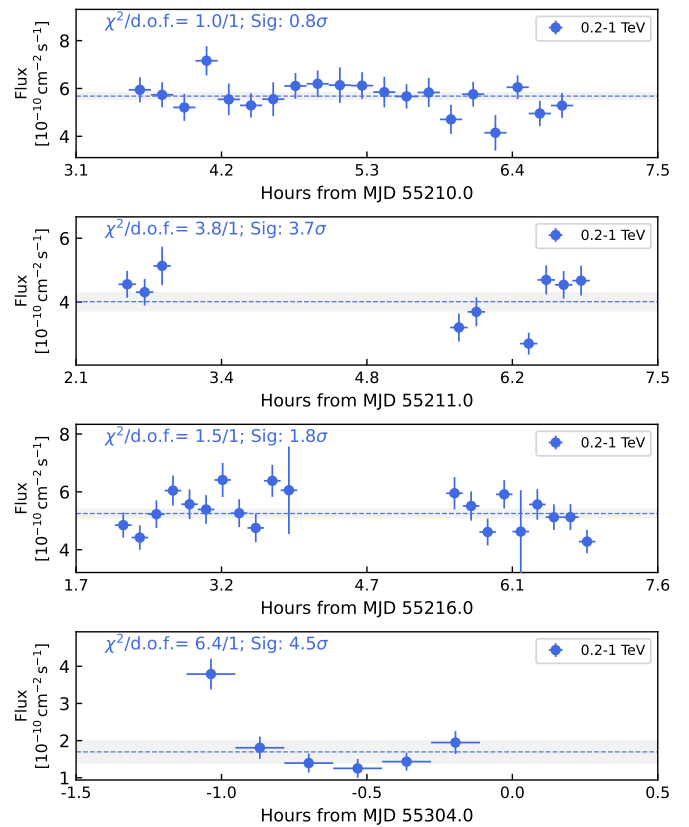


Fig. C.1: Intranight VHE variability in the two energy bands 0.2-1 TeV and >1 TeV. The data are binned in 10 min. The dotted line shows the constant fits for the 0.2-1 TeV band.

1170 plot and above 1 TeV in the right one. Both plots show a clear
1171 harder-when-brighter trend. The rise of the HR with the flux is
1172 steep for low fluxes but flattens at higher flux levels. In the right
1173 plot, the HR seems to remain constant with a rising flux above
 $\sim 3 \times 10^{-11} \text{ cm}^{-2} \text{ s}^{-1}$. The plot on the left shows similar behavior,
1174 but the overall scatter of the data is slightly higher. This flatten-
1175 ing harder-when-brighter-trend at VHE gamma rays is consistent
1176 with previous reports (e.g. Acciari et al. 2021). 1177

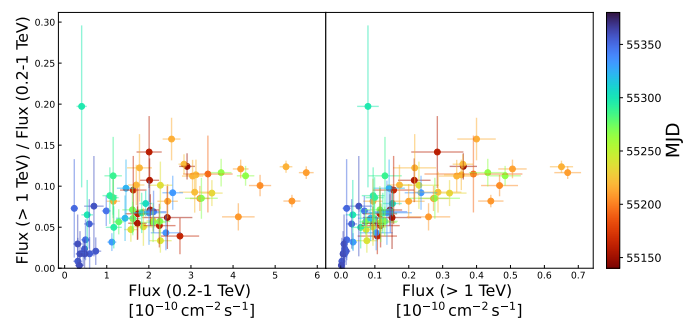


Fig. D.1: Hardness ratios as a function of the flux 0.2-1 TeV (left) and above 1 TeV (right) obtained by MAGIC. The color indicates the time of the observation in MJD.

1178 Fig. D.2 shows the HRs of the *Swift*-XRT observations as a
1179 function of the fluxes between 0.3-2 keV in the left and 2-10 keV
1180 in the right plot. At the end of the campaign, when the source is
1181 in a low state of activity, the HR goes as low as ~ 0.26 . Similar
1182 to the VHE data, a clear harder-when-brighter trend is visible.

1183 On the contrary, the HR does not show a clear flattening, but a
 1184 rather linear behavior. This is especially pronounced in the right
 1185 plot. In the left plot for the lower-energy fluxes, the data is more
 1186 scattered. The highest HR of ~ 1.55 , directly at the start of the
 1187 campaign, still seems to follow an almost linear trend. The HR
 1188 ratio corresponding to the highest flux values, however, is more
 1189 compatible with a flattening of the trend. Overall, the flattening
 1190 of the HR is much less pronounced than in the results from [Ac-
 1191 ciari et al. \(2021\)](#).

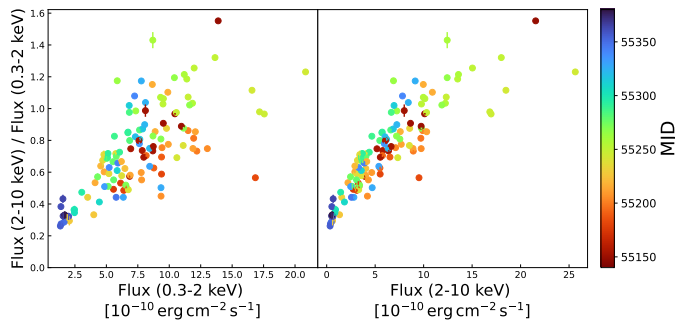


Fig. D.2: Hardness ratios as a function of the flux between 0.3-2 keV (left) and 2-10 keV (right) obtained by *Swift*-XRT. The color indicates the time of the observation in MJD.

visible, for instance, between December 2009 and mid-January 1227
 2010, or between mid-February 2010 and early March 2010 (see 1228
 Fig. 1), where no VHE gamma-ray observations are available, 1229
 while the densely *Swift*-XRT light curve unveils strong variabil- 1230
 ity. Since the normalization of the DCF depends on the stan- 1231
 dard deviation from the entire light curve and not only from the 1232
 VHE/X-ray simultaneous measurements (as is the case for the 1233
 Pearson coefficient), the DCF strategy, for this specific dataset is 1234
 biased towards lower values, given the strong X-ray variations 1235
 in periods without a VHE coverage. The mismatch in the cov- 1236
 erage between the X-ray and VHE light curves also generates a 1237
 larger spread in the DCF of the simulated light curves (used to 1238
 determine its significance), further reducing the significance of 1239
 the measured correlations. These effects were already reported in 1240
[Max-Moerbeck et al. \(2014\)](#). Therefore, we concluded that, for 1241
 this specific case of the X-ray and VHE gamma-ray light curves, 1242
 the DCF strategy is not adequate to properly quantify the magni- 1243
 tude of the correlation and its related significance. On the other 1244
 hand, the local cross-correlation function (LCCF; [Welsh 1999](#)) 1245
 provides an alternative approach to that of the DCF, since it also 1246
 takes into account the measurement uncertainties, but differently 1247
 to the DCF, the values are normalized with the standard devia- 1248
 tion from only the coincident measurements (analogous to the 1249
 Pearson coefficient). As a cross-check, we evaluated all corre- 1250
 lations estimated from the flux-flux plots in this work with the 1251
 LCCF, and we found that the values and significances are almost 1252
 identical to those obtained for the Pearson coefficient. 1253

1192 Appendix E: Estimating the significances of 1193 correlations

1194 We simulate a set of 100.000 uncorrelated pairs of light curves
 1195 for each combination of energy bands, following the previous
 1196 prescription, in Appendix B. To get the same degree of variabil-
 1197 ity at different frequencies as the real data, we use the PSDs ob-
 1198 tained in Sec. 4.2. The simulated light curves are generated with
 1199 a temporal precision matching the typical observation time of
 1200 the observations and then binned with the same temporal sam-
 1201 pling as the real data. We then compute the coefficient for each
 1202 pair. The resulting distributions are fitted with a Gaussian Kernel
 1203 model to approximate the probability density function (PDF).
 1204 Integration of the PDF above the coefficient of the real dataset
 1205 provides a p-value. It indicates the probability of finding uncor-
 1206 related datasets that have a correlation at least as extreme as the
 1207 one computed from the real dataset. We then translate the p-value
 1208 into a significance expressed in levels of 1σ . It must be empha-
 1209 sized that the standard approach for assessing the significance of
 1210 the Pearson coefficient under the assumption of two Gaussian-
 1211 distributed data sets is not applicable. The given datasets show
 1212 flux distributions with strong tails towards higher fluxes. Addi-
 1213 tionally, measurement uncertainties are not taken into account in
 1214 the standard method. We, therefore, rely on simulations to esti-
 1215 mate the significance, which gives a more robust and conserva-
 1216 tive estimate.

1217 Besides the Pearson correlation, many studies also make use
 1218 of the discrete correlation function (DCF; [Edelson & Krolik
 1219 1988](#)) to quantify the correlation between fluxes in two energy
 1220 bands. However, in this particular case of correlating the X-ray
 1221 and the VHE gamma-ray light curves, we found that the DCF ap-
 1222 proach is less sensitive and yields somewhat underestimated val-
 1223 ues for the correlation strength. The resulting underestimation of
 1224 the correlation occurs because the VHE and X-ray light curves
 1225 have very different temporal coverage, with the X-rays having
 1226 a much denser sampling with substantially fewer gaps. This is

Appendix F: Discrete correlation functions

This section presents the results of the DCF analysis referenced 1255
 in the main text. 1256

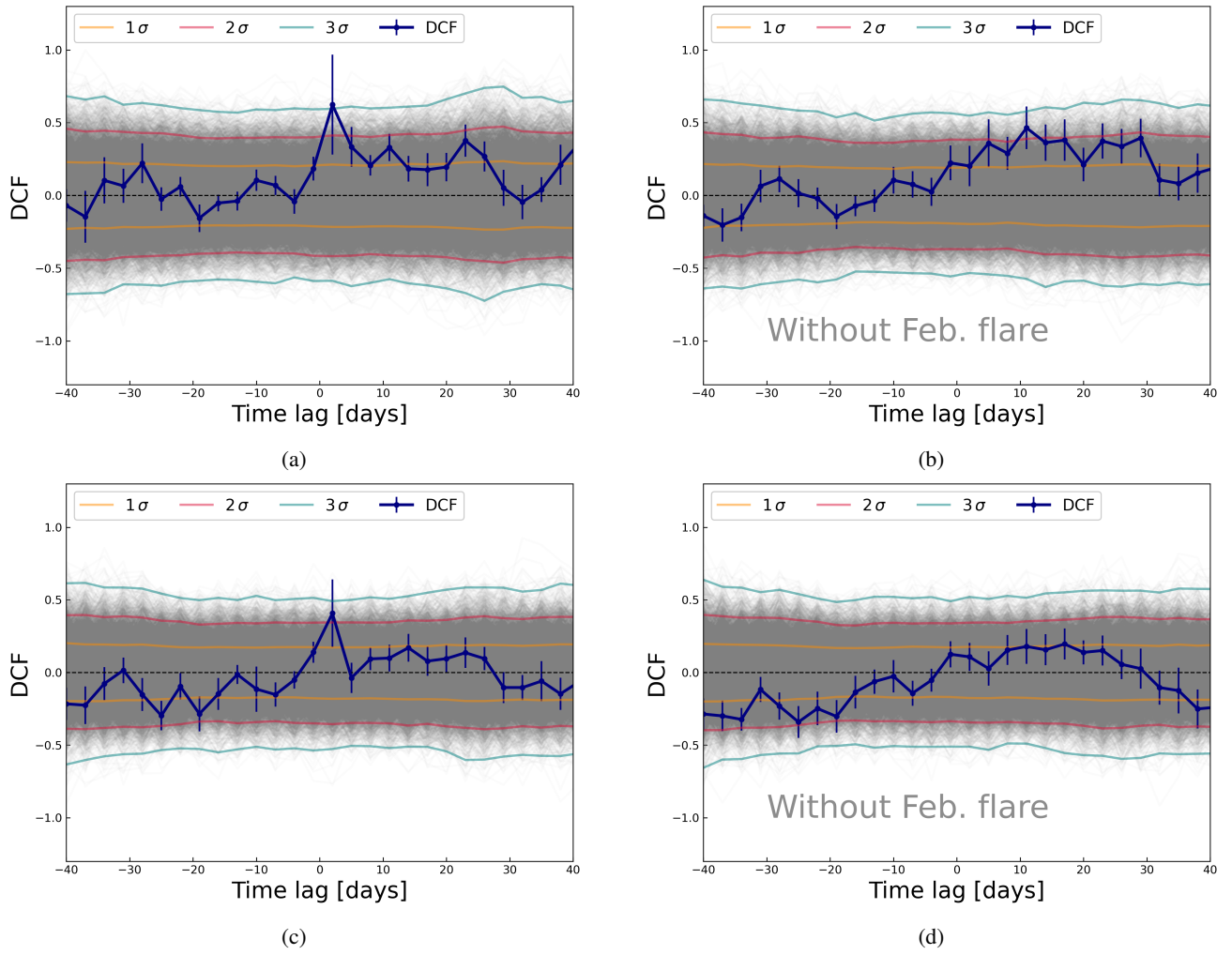


Fig. F.1: Discrete correlation function computed between the VHE gamma-ray fluxes above 0.2 TeV, as measured by MAGIC and VERITAS, and the HE gamma-ray fluxes measured by *Fermi*-LAT. The DCF is computed using a time bin of 3-days for a range of time lags between -40 to +40 days. The 1σ , 2σ , and 3σ confidence levels obtained by simulations are shown by the yellow, red, and green lines, respectively. (a) >0.2 TeV versus 3-300 GeV; (b) >0.2 TeV versus 3-300 GeV without the flare in February 2010; (c) >0.2 TeV versus 0.3-3 GeV; (d) >0.2 TeV versus 0.3-3 GeV without the flare in February 2010.

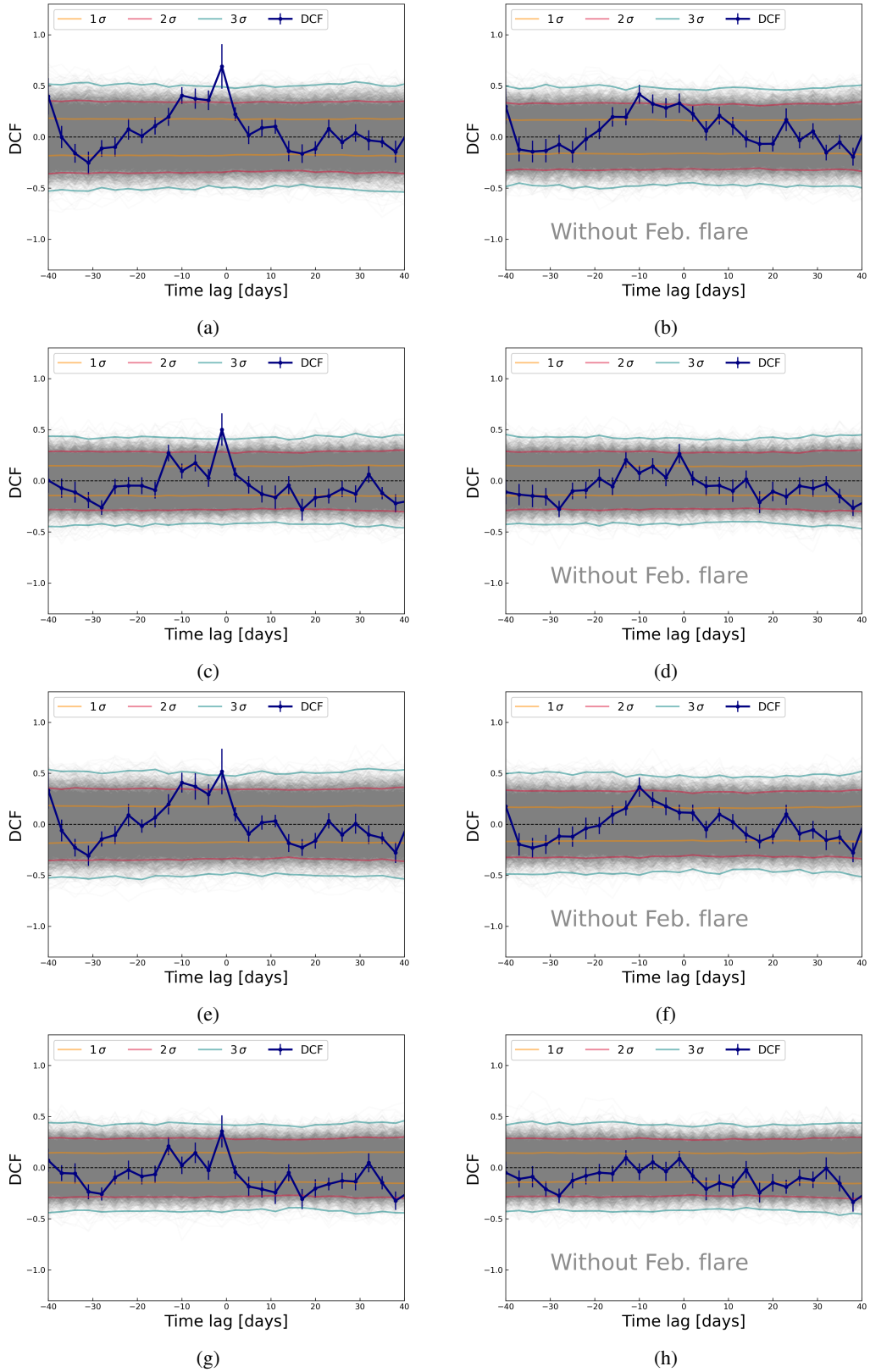


Fig. F.2: Discrete correlation function computed between two energy ranges provided by *Fermi*-LAT and *Swift*-XRT with and without the big flare in February using a binning of 3 days. It is computed for a range of time lags between -40 to +40 days. The 1σ , 2σ , and 3σ confidence levels obtained by simulations are shown by the yellow, red, and green lines, respectively. (a) 3-300 GeV versus 0.3-2 keV; (b) 3-300 GeV versus 0.3-2 keV without the flare in February 2010; (c) 0.3-3 GeV versus 0.3-2 keV; (d) 0.3-3 GeV versus 0.3-2 keV without the flare in February 2010; (e) 3-300 GeV versus 2-10 keV; (f) 3-300 GeV versus 2-10 keV without the flare in February 2010; (g) 0.3-3 GeV versus 2-10 keV; (h) 0.3-3 GeV versus 2-10 keV without the flare in February 2010.

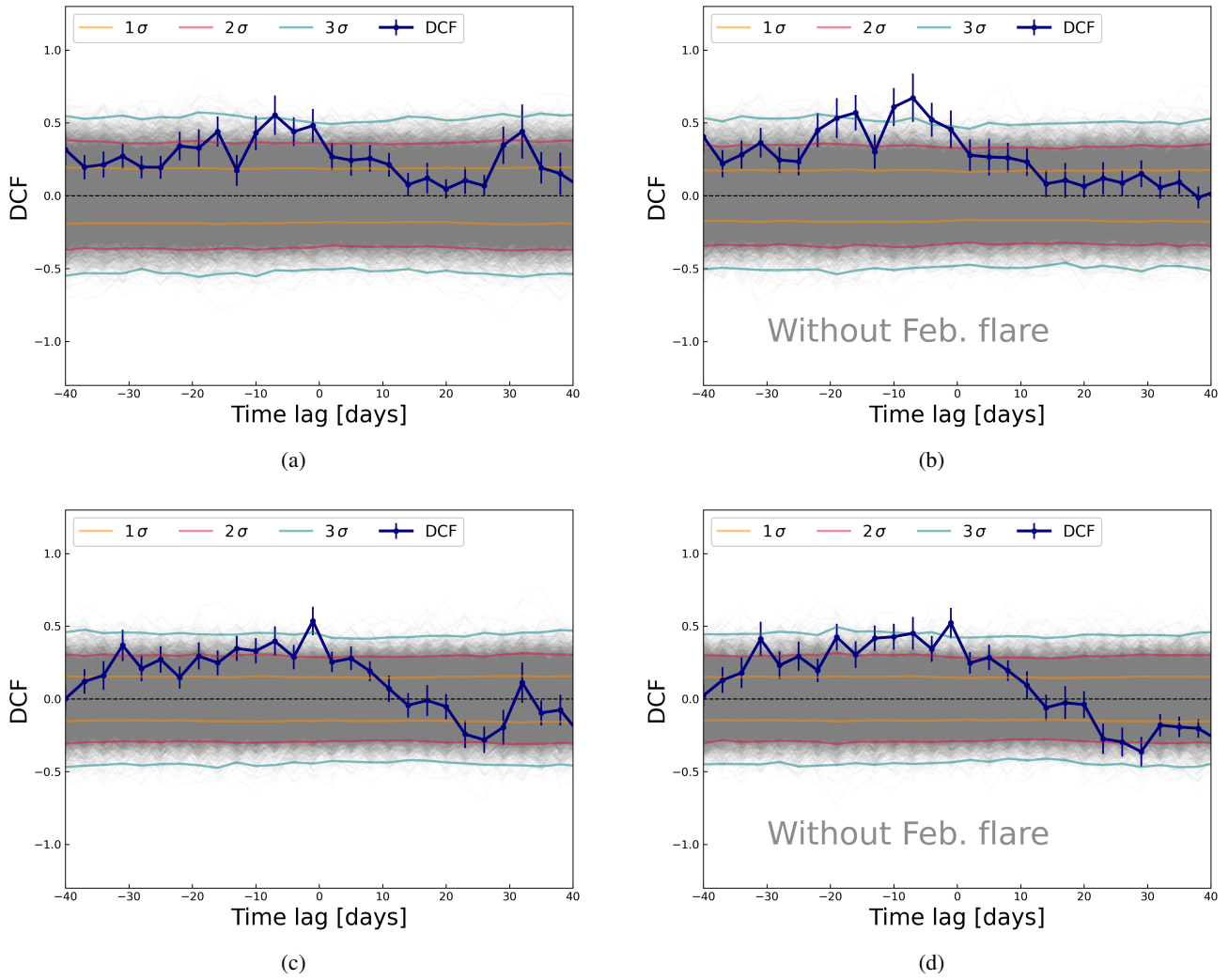


Fig. F.3: Discrete correlation function computed between the two energy ranges provided by *Fermi*-LAT and the W1 filter by *Swift*-UVOT without the big flare in February using a binning of 3 days. It is computed for a range of time lags between -40 to +40 days. The 1σ , 2σ , and 3σ confidence levels obtained by simulations are shown by the yellow, red, and green lines, respectively. (a) 3-300 GeV versus W1; (b) 3-300 GeV versus W1 without the flare in February 2010; (c) 0.3-3 GeV versus W1; (d) 0.3-3 GeV versus W1 without the flare in February 2010.

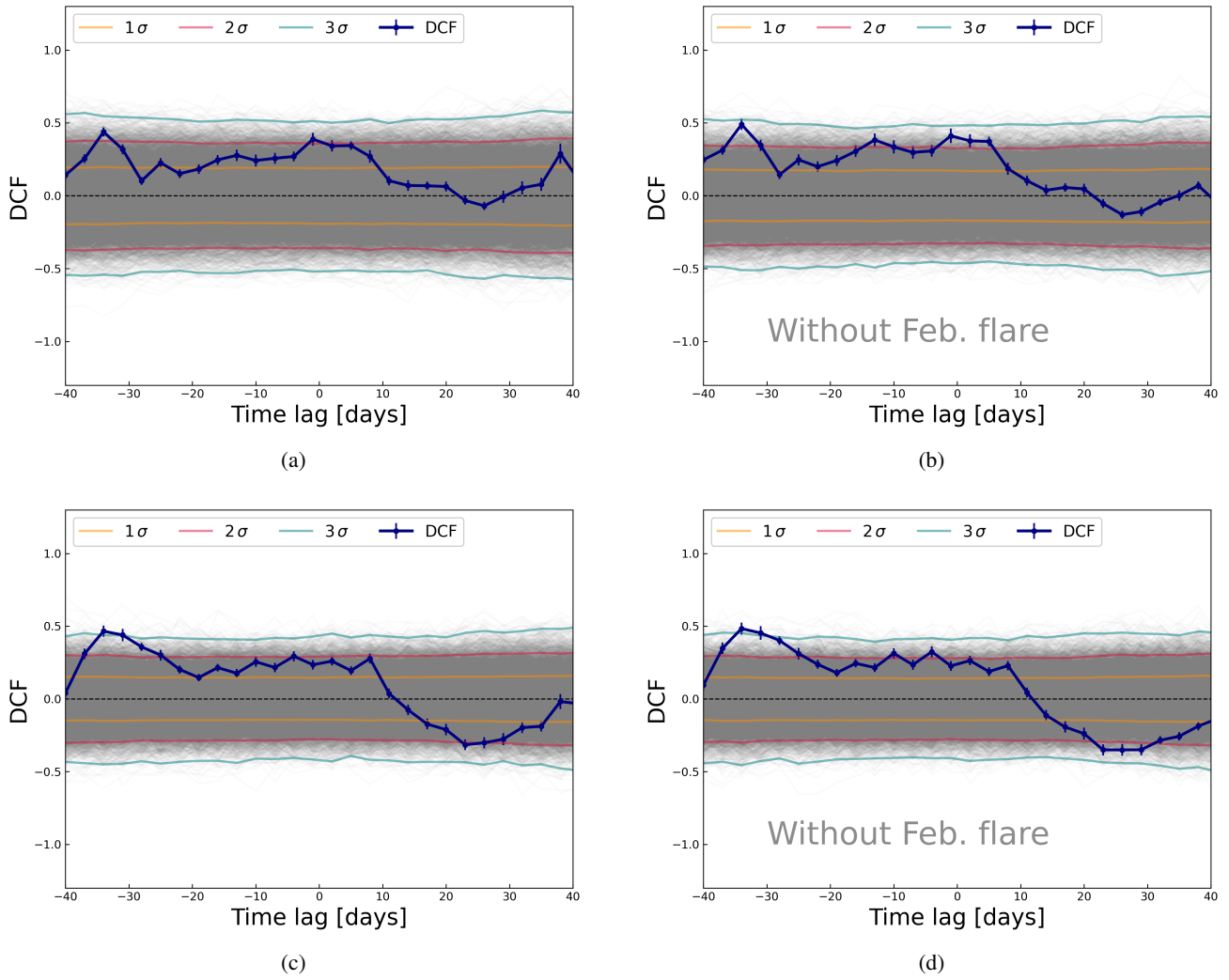


Fig. F.4: Discrete correlation function computed between the two energy ranges provided by *Fermi*-LAT and the R-band by GASP-WEBT without the big flare in February using a binning of 3 days. It is computed for a range of time lags between -40 to +40 days. The 1σ , 2σ , and 3σ confidence levels obtained by simulations are shown by the yellow, red, and green lines, respectively. (a) 3-300 GeV versus R-band; (b) 3-300 GeV versus R-band without the flare in February 2010; (c) 0.3-3 GeV versus R-band; (d) 0.3-3 GeV versus R-band without the flare in February 2010.